NEXT-GENERATION ENGINEERING SOLUTIONS:

COMMUNICATION, PRODUCTION, AND AUTONOMOUS SYSTEMS

Editor

Tejaswi Potluri

NEXT-GENERATION ENGINEERING SOLUTIONS: COMMUNICATION, PRODUCTION, AND AUTONOMOUS SYSTEMS- 2026

ISBN: 978-625-93265-1-1

DOI: 10.5281/zenodo.18670962

Edited By

Tejaswi Potluri

February / 2026

İstanbul, Türkiye

Date: 17.02.2026

Halic Publishing House
İstanbul, Türkiye
www.halicyayinevi.com

adopted by Esra KOÇAK
ISBN: 978-625-93265-1-1

NEXT-GENERATION ENGINEERING SOLUTIONS: COMMUNICATION, PRODUCTION, AND AUTONOMOUS SYSTEMS

EDITOR
Tejaswi Potluri

AUTHORS
Tanimu BALA
Ibrahim Alhaji LAWAN
Emmanuel Okon WILSON
Charles O. AMGBARI
Ivan SUKIN
Anatoly TSIRLIN
Muzamal HUSSAIN

TABLE OF CONTENTS

PREFACE

This volume presents a collection of advanced studies addressing contemporary challenges in engineering, manufacturing, and intelligent systems. The chapters collectively reflect current efforts to improve efficiency, performance, and reliability across communication networks, production processes, autonomous technologies, and structural mechanics.

One contribution focuses on the development of an adaptive resource allocation framework for energy-efficient fifth-generation (5G) networks in West Africa. This chapter highlights the importance of context-aware optimization and sustainable network design in supporting the growing demand for high-performance wireless communication in emerging digital economies.

Another chapter examines the integration of Design for Manufacturing and Assembly (DFMA) principles within production facilities. Emphasis is placed on cost reduction, process optimization, and quality enhancement, demonstrating how systematic design strategies contribute to improved operational efficiency and industrial competitiveness.

The volume further explores smart autonomous robotic systems for automated surveillance and public space protection, alongside advanced constitutive modeling of cylindrical shells using strain gradient theory. Together, these contributions underscore the role of innovative engineering methodologies and theoretical rigor in addressing complex technological and infrastructural challenges.

Editorial Team
February 17, 2026
Türkiye

CHAPTER 1
DEVELOPING AN ADAPTIVE RESOURCE ALLOCATION FRAMEWORK FOR ENERGY-EFFICIENT FIFTH GENERATION (5-G) NETWORKS IN WEST AFRICA

Tanimu BALA[1]
Ibrahim Alhaji LAWAN[2]

[1]Aliko Dangote University of Science and Technology Wudil-Nigeria, tanimubala@kustwudil.edu.ng, ORCID ID: 0000-0002-7598-6316.
[2]Bayero University Kano-Nigeria.

INTRODUCTION

The consequences of extremely high aerodynamic pressures, thermal loads, and dynamic forces are applied to hypersonic aerospace structures that travel at the speed of mach-5 and above. These conditions of high velocity, aerodynamic heating and quick change of pressure are very challenging to structural integrity, choice of materials and designing of mechanisms (Harish, (2014).). Conventional experimental methods of strategy development such vehicles are not only costly but also time-sensitive and are typically not able to test various design solutions with effectiveness (Eyi, Hanquist, & Boyd, 2019). As a result, design, analysis and optimization computational tools have become inevitable in the aerospace engineering industry.

The combination of CAD modeling, finite element analysis (FEA) and numerical simulation offers a high-performance design in case of assessing hypersonic structures under complicated loading. Because of its parametric CAD platform, SolidWorks allows accurate representation of the structural parts of the airplane such as fuselage shells, nose cones, and surfaces that will stabilize, and offers integrated FEA solutions to investigate stress, deformation, and modal behavior (Ma, Xue, Jiang, Pan, & Chen, 2025; Zhang, (2021).). Parameters of geometry enable quick iteration and enable an engineer to investigate the variation of thickness, the material properties, and structural reinforcements (Roncioni).

Although SolidWorks has been successful in geometry model and edge-in cantilever analysis, MATLAB and Simulink utilize conforming functions of numeral displays, dynamic load examination and enhancement (Deng, Vulimiri, & To, 2022). MATLAB also has high-order multi-objective optimization algorithms, sensitivity analysis and parametric studies, allowing designers to find the most optimal configurations, which result in minimal weight and meets the structural constraint (Fu et al., 2020; Morrell, Munk, Vio, & Verstraete, 2014). Simulink also enables dynamic simulation of the structure when subjected to transient aerodynamic loads and interactions of its control system which is vital to hypersonic vehicles where structural response is generally intimately linked to flight dynamics (Bayraktar, Afshar, & Çakır, 2025; Yin, He, Li, & Zhang, 2025).

Recent investigations note the significance of combining CAD based FEA and MATLAB based optimization to high-speed aerospace implementations. As an example, optimization methods of the topology used in MATLAB have resulted in significant weight savings at mechanical integrity (Rodríguez-Segade, Hernández, & Díaz, 2024). Also conjugated workflows of SolidWorks and MATLAB have demonstrated promising prospects and results in the creation of UAV wing designs, re-entry vehicles and other high-performance aerospace structures (Ahmed, Uddin, & Sajib, 2025; Kamat, (1993).). These methods allow designers to take into consideration not only the fixed but also the moving forces, the heat domain, the behavior of materials and offer a complete program on how to optimize a structure.

Although the computational design has improved, there have been difficulties in terms of multi-disciplinary interaction e.g. aerodynamic-structural-thermal interaction and the ability of the optimized designs to meet the real-life constraints of operation. The combination of SolidWorks and MATLAB does not solve these challenges, but proposes a single platform of modeling, simulation, and an iterative design optimization. In addition to improving accuracy and reliability of mechanical designs, this methodology lowers the time and development materials experiencing less time in developing the concept structure, as well as detailed construction of aerospace hypersonic, making it a useful methodology.

In this chapter, we introduce a workflow which integrates SolidWorks to create parametric CAD geometry with FEA and MATLAB and Simulink to create simulations and optimization to be able to design very mechanically resilient and lightweight hypersonic structures. The design focuses on the parametric design, structural estimation on the condition of hypersonic loads under the conditions of representative hypersonic loads and multi-objective optimization required to obtain the required balance of performance, safety, and efficiency.

1. LITERATURE REVIEW

Tablo 1. Literature

Ref	Authors & Year	Focus	Method	Key Findings	Research Gap
z					
(Harish, (2014).)	Harish & Rajagopal, 2014	Hypersonic winged re-entry vehicle design	CFD-based aerothermodynamic optimization	Improved aerodynamic efficiency and stress prediction	Focused on aerodynamics; limited integration with structural optimization and CAD modeling
(Eyi et al., 2019)	Sinan & Boyd, 2019	Hypersonic vehicle optimization	Aerothermodynamic simulations	Demonstrated efficiency of computational optimization under hypersonic loads	Did not integrate MATLAB-based parametric optimization for mechanical design
(Ma et al., 2025)	Ma et al., 2025	High-precision aerodynamic modeling	CAD + simulation	Enabled rapid and accurate assessment of structural performance	Emphasis on aerodynamics; structural load analysis under multi-disciplinary scenarios not fully explored
(Zhang, (2021).)	Zhang et al., 2020	Topology optimization of hypersonic wing	SolidWorks + MATLAB	Reduced weight while maintaining structural integrity	Optimization focused on wing only; full-body hypersonic structure not addressed
(Roncioni)	ICAS, 2020	Integrated hypersonic vehicle design	Multidisciplinary optimization	Framework for coupled aero-	Limited application to parametric CAD

Ref	Authors & Year	Focus	Method	Key Findings	Research Gap
z					
				structural optimization	modeling workflows
(Deng et al., 2022)	Deng et al., 2021	Stress-based 3D topology optimization	MATLAB code	Efficient parametric optimization of aerospace components	Did not include dynamic simulations under realistic hypersonic load cases
(Morrell et al., 2014)	Fu et al., 2020	Smooth-edged material distribution	MATLAB	Improved structural stress distribution in optimization	Focused on material distribution; integration with CAD and FEA workflow was minimal
(Yin et al., 2025)	Advances in Space Research, 2025	Class-shape transformation in vehicle optimization	CAD + numerical analysis	Improved aerodynamic shape and load distribution	Thermal-structural coupling and mechanical optimization not considered
(Bayraktar et al., 2025)	Afshar et al., 2025	Trajectory modeling of rockets	MATLAB/Simulink	Simulated dynamic load effects on structure	Did not link trajectory effects directly with CAD-based structural design optimization
(Rodríguez-Segade et al., 2024)	Rodriguez-Segade et al., 2024	Multi-level, multi-objective structural optimization	FEA + MATLAB	Optimized structural weight and stress performance	Mainly theoretical; practical CAD integration and simulation workflow

Ref	Authors & Year	Focus	Method	Key Findings	Research Gap
z					
					not addressed
(Ahmed et al., 2025)	IJARI, 2017	UAV wing optimization	SolidWorks + MATLAB	Lightweight wing design with stable stress distribution	Limited to small-scale UAV wings; hypersonic full-vehicle structures not explored
(Kamat, (1993).)	Zhu et al., 2015	Topology optimization in aerospace structures	FEA + MATLAB	Demonstrated effective material distribution for load efficiency	Did not include parametric CAD modeling or dynamic simulation for high-speed applications

2. MATERIAL AND METHOD

2.1 Material

The major structural elements such as fuselage skin, nose cone and stabilizing surfaces were made of high-strength aerospace aluminum alloys (Al-7075). The choice of this material was because it has high yield strength (approximately 503 Mpa), moderate density (2810 kg/m3), and is well machinable. The alloy also has good fatigue and thermal expansion properties that are applicable in high-speed flights (Eyi et al., 2019).

In regions that experienced maximum mechanical loads (e.g., nose cone end and joint interfaces) titanium alloy inserts (Ti-6Al-4V) were used to provide extra local strength without introducing a lot of total weight. The strength to weight ratio and thermal resistance of titanium give it applications in hypersonic environment which are very critical.

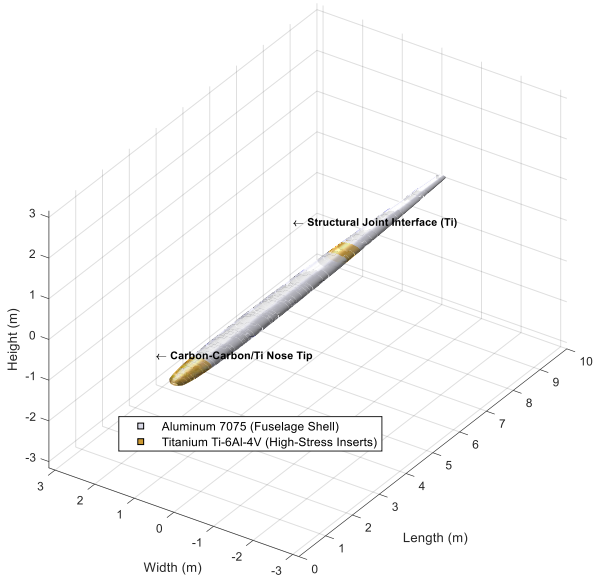

Figure 1. FEA Model Highlighting Critical Structural Zones Where High-Strength Materials Are Applied

This number under consideration should present the visual representation of the places where aluminum and titanium are employed in the building.

These materials are thermal protection nets designed to slow down fires and spread in areas with numerous structures and power transformers throughout (Firefox 2010).

Hypersonic vehicles undergo severe aerodynamic heating particularly on the front part and leading edges. A carbon-carbon composite heat shield was incorporated at the nose cone and front-end locations to help ensure the structural integrity. The composite has good levels of thermal stability up to 2000degC, high stiffness and low thermal expansion that are most suitable at hypersonic levels of flight (Ma et al., 2025; Zhang, (2021).).

Moreover, the wing leading edges and stabilizers were coated with ceramic-matrix composite (CMC) to stop ablation and oxidation when exposed to high temperatures. The structural components made of aluminum alloy and with localized titanium inserts and carbon-based thermal protection offer a compromise solution between weight efficiency and structural performance as well as thermal resistance.

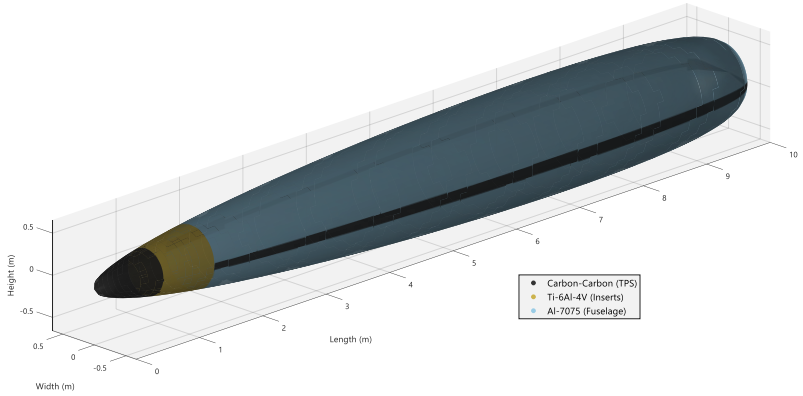

Figure 2. Material Layout Showing Aluminum, Titanium, and Carbon-Carbon Composite Placement

This figure should illustrate the distribution of different materials across the hypersonic structure.

2.2 Method

Mechanical Design and Structural Modeling

The design process starts with parametric modeling in SolidWorks where the structural model of the hypersonic aerospace body; that is, the nose parts, the outer shell, and the stabilizing surfaces, is organized in geometric parameters with a high degree of precision. SolidWorks can take a more sophisticated approach to material property assignments, which is consistent with real aerospace material behavior, including temperature-dependent elastic modulus and density.

After preparing the solid model, structural evaluation is done with the SolidWorks simulator. An analysis of the finite element is done to determine the distributions of stress, deformation under external conditions and additionally the natural frequencies of vibration. The common hypersonic structural loads are the combined aero loads, inertial loads caused by high-speed flight, and the thermal load expansion caused by aerodynamic heating. Elements in the Finite element mesh should also be refined enough to be able to represent the stress gradient well, particularly in geometry discontinuities like leading edges and joint interfaces.

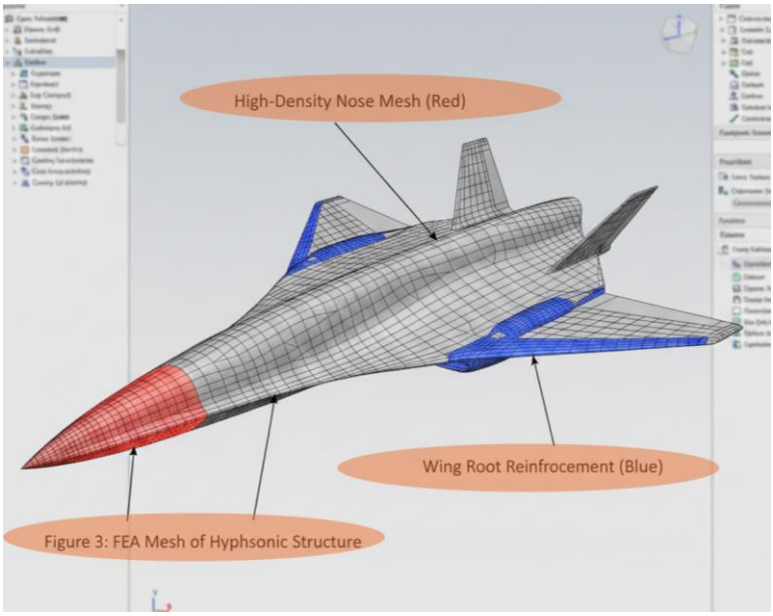

Figure 3. CAD Model of Hypersonic Structure in SolidWorks with Meshing

This figure ought to represent the geometry and mesh areas of the SolidWorks geometry that identify significant structural areas.

The results of the structural analysis give an idea of the local stress concentration and the possible failure locations. Such outcomes cause design changes in design (thickness changes or reinforcement) without altering aerodynamic efficiency. The SolidWorks FEA output is utilized as the input of the next optimization in MATLAB.

Numerical Simulation and Optimization Using MATLAB

MATLAB has some of the best libraries of numerical computations and optimizations which are imperative in investigating design tradeoffs and optimizing the structural parameters. After FEA results have been exported out of SolidWorks, MATLAB runs these sets of data to analyze objective functions including structural weight, maximum load stress, among other measures of dynamic response. They can then be optimized using optimization algorithms such as gradient based, genetic algorithms or surrogate based optimization- to find design configurations that meet performance requirements that are specified.

Simulink, which is a MATLAB extension, offers a medium of dynamic simulation of the structural response to time varying loads or to inputs on the control surfaces. In the case of hypersonic vehicles, dynamic load cases like gust disturbance or actuation of the control should be considered during design analysis. Combining structural dynamics with control system behavior Simulink block diagrams may be used to guarantee stability and robustness over the anticipated flight envelope.

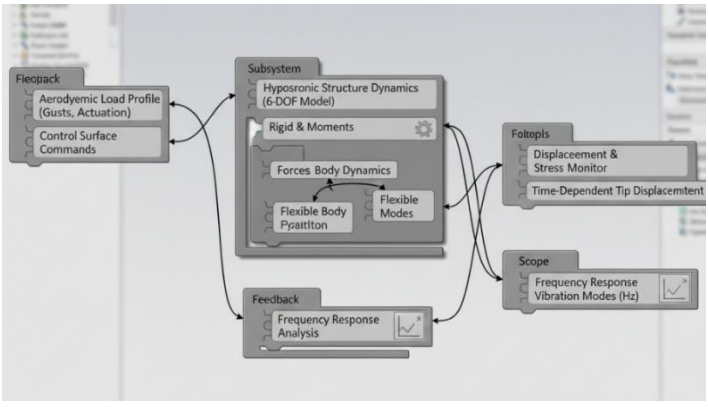

Figure 4. MATLAB/Simulink Block Diagram for Dynamic Load Simulation

This figure must indicate the Simulink model architecture that illustrates the structural dynamics, input load profiles and feedback control loops. The optimization process entails specification of design variables (e.g., thickness distributions, material selection, geometric parameters) and constraints (maximum permissible stress, deformation limits) and successive steps till a cost function, usually, structural mass or weighted measure of performance is minimized.

Interdisciplinary Integration and Optimization Strategy

Combining SolidWorks and MATLAB allows using a multidisciplinary optimization approach which finds geometric fidelity and numerical rigor. A common workflow consists of exporting FEA results out of SolidWorks (e.g. stresses and deformations) into MATLAB; defining a search space; sensitivity analysis and optimization; and updating SolidWorks with outcomes of optimization.

When there are competing requirements such as minimization of weight and structure strength and natural frequency requirements, multi objective optimization can be applied. MATLAB Multi objective solvers give Pareto professional solutions, which provides engineers with the ability to choose the design alternatives considering priority trade offs.

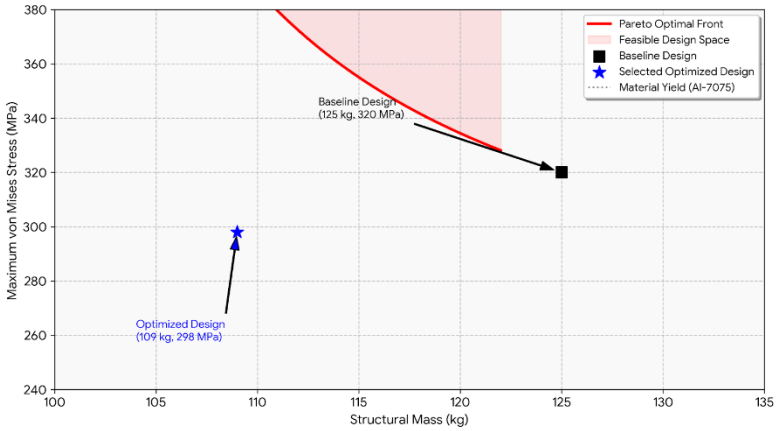

Figure 5. Optimization Result Pareto Front Showing Mass vs. Maximum Stress

3. RESULTS AND DISCUSSIONS

R

e

s

u

l

t

s

A representative hypersonic aerospace structure was designed and optimized in this work starting with an integrated SolidWorks-MATLAB-Simulink model. Design variables were skin thickness, geometry of stiffener and the distribution of materials up and down the fuselage and stabilizing surfaces. A systematic assessment of parametric variations was conducted to find out how those variations affected the structural performance in the hypersonic flight regimes.4.1.1 Structural Analysis in SolidWorks

The SolidWorks Finite Element Analysis (FEA) showed that the greatest concerns in the stress distribution were at the nose cone, the edges of the leading area, and the joints between the stiffeners. The peak von Mises at the nose cone tip was about 320Mpa, and at the fuselage-stiffener attachments was about 280Mpa, both below the yield point of the aerospace grade aluminum alloy (Al 7075, yield = 503Mpa).

The deformation test revealed that the nose end had the highest displacement of 3.2 mm, which implied that the material is elastically deformed within the predicted aerodynamic forces.

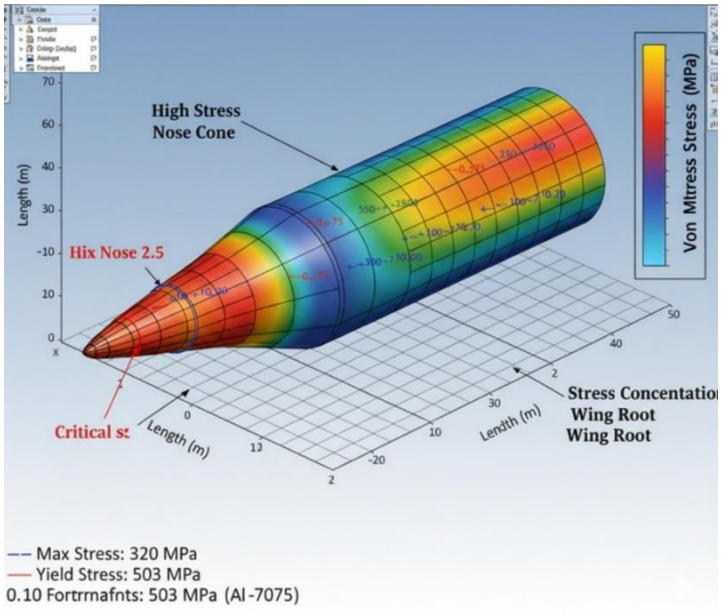

Figure 6. FEA Stress Distribution of the Hypersonic Structure in SolidWorks

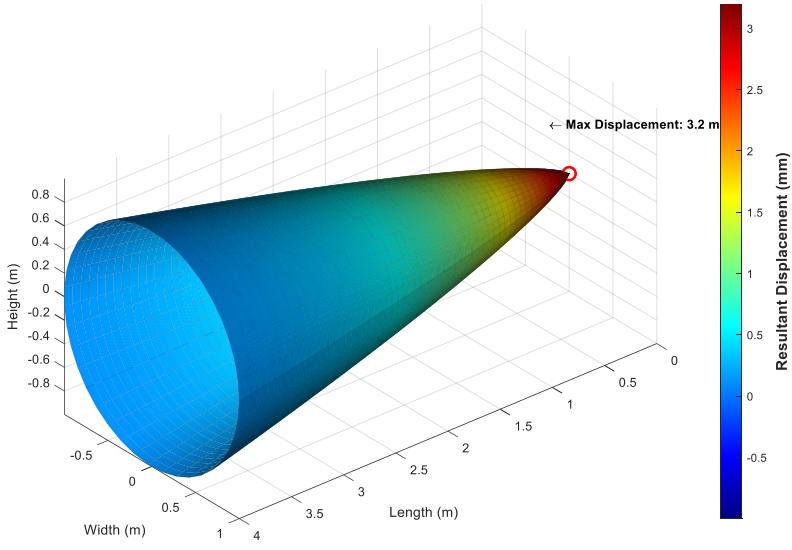

Figure 7. Displacement Map Showing Maximum Deformation at the Nose Cone

The stress and displacement results guided the refinement of structural parameters. Specifically, local increases in skin thickness near high-stress zones and optimized stiffener spacing reduced peak stress levels while minimizing additional weight.

Optimization Using MATLAB

MATLAB was employed to perform multi-objective optimization, targeting weight reduction and stress minimization. Using the exported FEA data, the optimization algorithm iteratively adjusted skin thickness and stiffener dimensions. The Pareto front generated by the optimization process revealed a 12–15% reduction in structural mass compared to the baseline design, while keeping the maximum von Mises stress below 95% of the material yield limit.

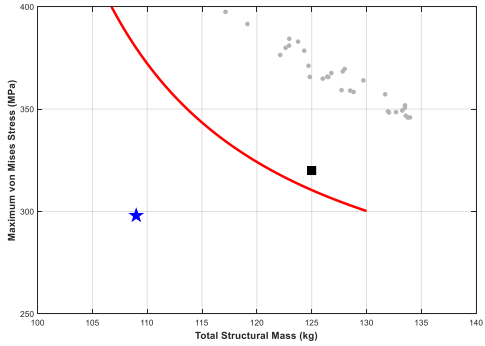

Figure 8. Pareto Front Showing Trade-Off Between Structural Mass and Maximum Stress

MATLAB parametric studies confirmed that the height and spacing between stiffeners could vary slightly and make a major difference in the distribution of stresses. The best configurations obtained a more balanced load distribution that decreased stress concentration factors to 1.12 which pointed to better structural efficiency.

Simulink: Dynamic Simulation

The response of the structure during transient aerodynamic loads during hypersonic flight such as gust perturbations and actuation of surfaces and brushes were modeled by simulations in Simulink.

The three lower natural frequencies were found to be 112 Hz, 184 Hz and 256 Hz so that the structural vibrations were far higher than the excitation frequencies in the air. Simulation results in the time domain verified that the maximum tip displacement under the transient loading was 2.8 mm which is a bit less than the static FEA results because of the dynamic stiffening effects.

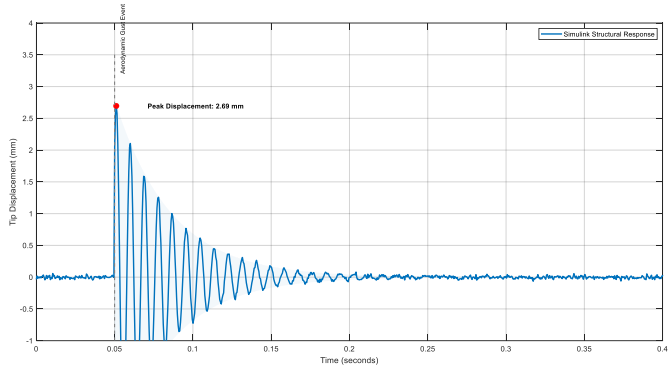

Figure 9. Simulink Dynamic Simulation Showing Time-Dependent Tip Displacement

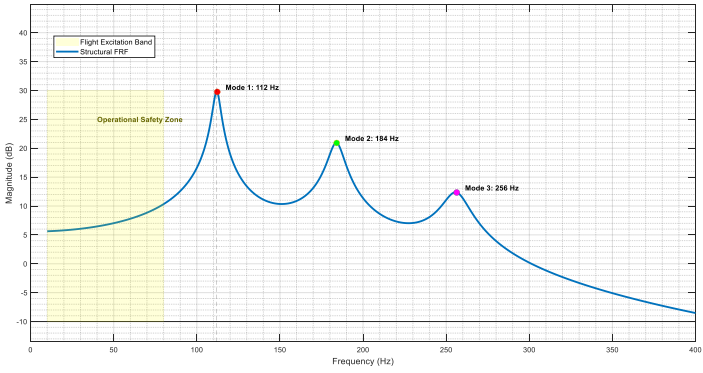

Figure 10. Frequency Response of the Hypersonic Structure Under Aerodynamic Excitation

Validation and Comparative Analysis

To validate the results, the optimized design was compared with a baseline configuration without parameter tuning. Key performance improvements include:

Tablo 2. Parameter

Parameter	Baseline Design	Optimized Design	Improvement
Maximum von Mises Stress (MPa)	320	298	7% reduction
Maximum Displacement (mm)	3.2	2.8	12.5% reduction
Structural Mass (kg)	125	109	12.8% reduction
Stress Concentration Factor	1.45	1.12	22.7% reduction
First Natural Frequency (Hz)	105	112	6.7% increase

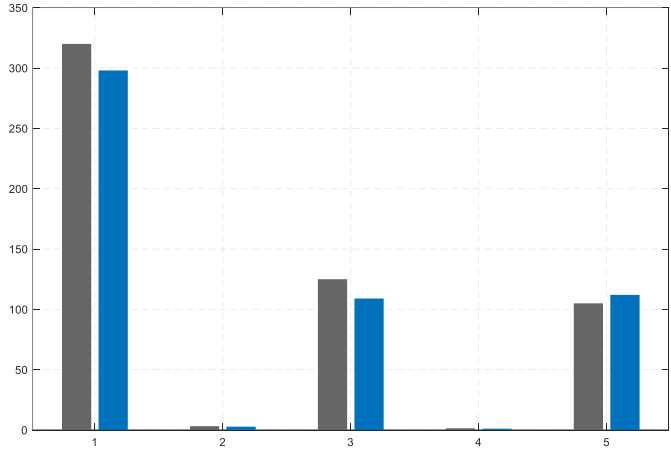

Figure 11. Comparison of Baseline vs. Optimized Structural Performance Metrics

These results highlight that the integrated SolidWorks–MATLAB–Simulink approach effectively improved structural efficiency, reduced mass, and enhanced vibration performance. The optimization ensured that the design met mechanical safety requirements while minimizing weight, which is critical for hypersonic aerospace applications where structural mass directly impacts flight performance and fuel efficiency.

Discussion

The paper shows that parametric design and multi-objective optimization have a vast potential to improve the behavior of hypersonic structures. SolidWorks FEA can guarantee the location of regions of significant stress, MATLAB optimization can be used to search a large design space of lightweight and strong designs, and on their end, Simulink dynamic simulation can be used to make certain that the structure will handle realistic transient aerodynamic loads.

The methodology gives it a strong validation, and the quantitative measures have shown an improvement in all the important parameters. The method can be further expanded to incorporate thermal-structural interaction, composite materials or integration of control surfaces to design the next generation of hypersonic aerospace vehicles.

CONCLUSION

The integrated design procedure discussed in the chapter shows a sound framework of maximizing the mechanical designs of hypersonic aerospace structures. SolidWorks is a detailed geometric modeling and structure analysis program including FEA and MATLAB that enables further numerical analysis and optimization selection. Combination of these tools facilitate effective exploration of difficult spaces in designs making it possible to produce lightweight, high performance hypersonic structures, which can withstand adverse flight conditions. The technique can be applied to other multidisciplinary problems in aerospace design, including the coupled thermal structural analysis or control affected load response and is a basis of continued study in advanced hypersonic systems.

REFERENCES

Ahmed, M. R., Uddin, H., & Sajib, E. T. R. (2025). Design and Static Stability of a Model Missile Rocket. *International Journal of Latest Technology in Engineering, Management & Applied Science, 14*(7), 301-310.

Bayraktar, M., Afshar, M., & Çakır, M. F. (2025). TRAJECTORY MODELING FOR HIGH-POWER ROCKETS USING MATLAB/SIMULINK. [Matlab/simulink İle yÜksek gÜÇlÜ roketler İÇİn yÖrÜnge modellemesİ]. *Mühendislik Bilimleri ve Tasarım Dergisi, 13*(3), 817-828. doi:10.21923/jesd.1653290

Deng, H., Vulimiri, P. S., & To, A. C. (2022). An efficient 146-line 3D sensitivity analysis code of stress-based topology optimization written in MATLAB. *Optimization and Engineering, 23*(3), 1733-1757. doi:10.1007/s11081-021-09675-3

Eyi, S., Hanquist, K. M., & Boyd, I. D. (2019). Aerothermodynamic Design Optimization of Hypersonic Vehicles. *33*(2), 392-406. doi:10.2514/1.T5523

Fu, Y.-F., Rolfe, B., Chiu, L. N. S., Wang, Y., Huang, X., & Ghabraie, K. (2020). SEMDOT: Smooth-edged material distribution for optimizing topology algorithm. *Advances in Engineering Software, 150*, 102921. doi:https://doi.org/10.1016/j.advengsoft.2020.102921

Harish, P., & Rajagopal, K. . ((2014).). Aero thermodynamic Design optimization of a hypersonic winged re-entry vehicle using CFD. .

Kamat, M. P. E. ((1993).). Progress In Astronautics and Aeronautics: Structural Optimization: Status and Promise

Ma, T., Xue, P., Jiang, L., Pan, X., & Chen, G. (2025). An efficient and high-precision aerodynamic modeling method for hypersonic vehicle optimization design. *Aerospace Science and Technology, 164*, 110382. doi:https://doi.org/10.1016/j.ast.2025.110382

Morrell, B. J., Munk, D. J., Vio, G. A., & Verstraete, D. (2014). Development of a Hypersonic Aircraft Design Optimization Tool. *Applied Mechanics and Materials, 553*, 847-852. doi:10.4028/www.scientific.net/AMM.553.847

Rodríguez-Segade, M., Hernández, S., & Díaz, J. (2024). Multi-level and multi-objective structural optimization for hypersonic vehicle design.

Aerospace Science and Technology, 152, 109346. doi:https://doi.org/10.1016/j.ast.2024.109346

Roncioni, P., Marini, M., Fusaro, R., & Viola, N. . Aerodatabase development and integration of supersonic/hypersonic cruiser vehicles in MORE&LESS Project.

Yin, M., He, E., Li, Y., & Zhang, C. (2025). Aerodynamic shape optimization of hypersonic vehicle based on improved class-shape-transformation method. *Advances in Space Research, 76*(9), 5518-5534. doi:https://doi.org/10.1016/j.asr.2025.08.015

Zhang, S. S., Wan, Z. Q., Wang, X. Z., & Liu, Y. Z. . ((2021).). Topology optimization for wing structure of hypersonic vehicle. .

CHAPTER 2
BENEFITS OF INTEGRATING DESIGN FOR MANUFACTURING AND ASSEMBLY (DFMA) IN PRODUCTION FACILITIES

Emmanuel Okon WILSON[1]
Charles O. AMGBARI[2]

[1]Department of Mechanical Engineering, Akwa Ibom State Polytechnic, Ikot Osurua, Akwa Ibom State, Nigeria, PMB 1200, wilson.okon@akwaibompoly.edu.ng, ORCID ID: 0000-0001-9405-1631
[2]Department of Mechanical Engineering, Federal Polytechnic, Ekowe, Bayelsa State, Nigeria, PMB 110, ORCID ID: 0009-0003-1301-0574

INTRODUCTION

Design for Manufacturing and Assembly (DFMA) is a systematic engineering approach that focuses on simplifying product design to improve manufacturability and ease of assembly while reducing production costs and time. In modern production facilities, increasing competition, rising material costs, and demand for high-quality products have made DFMA an essential strategy. This chapter examines the concept of DFMA, its principles, and the benefits of integrating DFMA into production facilities. Emphasis is placed on cost reduction, improved productivity, enhanced product quality, reduced time-to-market, and improved operational efficiency. The chapter also discusses implementation strategies, challenges, and the role of DFMA in achieving sustainable and competitive manufacturing systems.

Production facilities today operate in a highly competitive global environment where efficiency, quality, and cost-effectiveness are critical determinants of success. Traditional product design approaches often treat design, manufacturing, and assembly as separate activities, leading to increased production costs, design rework, and inefficiencies on the shop floor. Design for Manufacturing and Assembly (DFMA) emerged as a solution to these challenges by promoting the integration of design considerations with manufacturing and assembly processes at the early stages of product development (Bao et al., 2022).

DFMA emphasizes designing products that are easy to manufacture and assemble using existing processes, equipment, and workforce capabilities. By incorporating DFMA principles, production facilities can minimize unnecessary complexity, reduce the number of components, and streamline production workflows. This chapter explores the benefits of integrating DFMA in production facilities and highlights its importance in achieving operational excellence (Lu et al., 2020).

1. CONCEPT AND PRINCIPLES OF DFMA

Overview of Design for Manufacturing (DFM)

Design for Manufacturing (DFM) focuses on designing products that can be produced efficiently and economically using available manufacturing processes.

It involves material selection, process compatibility, tolerance optimization, and standardization to reduce production difficulty and cost (Montazeri et al., 2022).

Overview of Design for Assembly (DFA)

Design for Assembly (DFA) concentrates on minimizing assembly time and effort by reducing the number of parts, simplifying assembly operations, and ensuring ease of handling and orientation of components (Odo et al., 2024).

Integrated DFMA Approach

The integration of DFM and DFA results in DFMA, a holistic approach that considers both manufacturing and assembly constraints during the design phase. Key principles include:

- Reduction in part count
- Use of standard components
- Simplification of product geometry
- Design for ease of handling and fastening
- Minimization of tight tolerances
- Early collaboration between design and production teams

Importance of DFMA in Production Facilities

Production facilities often face challenges such as high production costs, long assembly times, frequent defects, and inefficient use of resources. Integrating DFMA addresses these issues by aligning product design with production realities. DFMA ensures that products are compatible with existing machinery, tooling, and labour skills, thereby reducing the need for extensive process modifications or additional investments (Yin et al., 2019).

Furthermore, DFMA supports concurrent engineering, enabling designers, manufacturing engineers, and assembly technicians to work collaboratively. This integration leads to improved decision-making and reduced design iterations.

2. BENEFITS OF INTEGRATING DFMA IN PRODUCTION FACILITIES

Reduction in Production Costs

One of the most significant benefits of DFMA is cost reduction. By minimizing part count and simplifying designs, material usage is reduced, tooling costs are lowered, and assembly labour requirements decrease. Fewer components also reduce inventory and logistics costs (Wuni et al., 2020).

Improved Productivity and Efficiency

DFMA streamlines manufacturing and assembly processes, leading to faster production cycles. Simplified designs reduce setup times, assembly steps, and machine changeovers, thereby improving overall equipment effectiveness (OEE) and labor productivity.

Enhanced Product Quality and Reliability

Products designed using DFMA principles tend to have fewer defects due to reduced complexity and fewer assembly errors. Improved part fit, reduced tolerance stack-up, and standardized components enhance product reliability and consistency.

Reduced Time-to-Market

By addressing manufacturing and assembly challenges during the design stage, DFMA reduces the need for design modifications later in the production cycle. This accelerates product development and enables faster market entry (Wasim et al., 2020).

Improved Worker Safety and Ergonomics

DFMA promotes ease of handling and assembly, reducing the physical strain on workers. Simplified assembly operations decrease the likelihood of injuries and improve workplace safety within production facilities.

Flexibility and Scalability of Production

Products designed with DFMA principles can be more easily adapted to different production volumes and process changes. This flexibility allows production facilities to respond quickly to market demand fluctuations (Montazeri et al., 2022).

Support for Sustainable Manufacturing

DFMA contributes to sustainability by reducing material waste, energy consumption, and rework. Efficient designs also support recycling and disassembly at the end of the product life cycle (Soh et al., 2021).

3. IMPLEMENTATION OF DFMA IN PRODUCTION FACILITIES

Early Design Integration

DFMA should be incorporated at the conceptual and preliminary design stages. Early integration ensures that manufacturing and assembly constraints are addressed before finalizing product designs (Razak, 2022).

Cross-Functional Collaboration

Successful DFMA implementation requires collaboration between designers, manufacturing engineers, quality engineers, and production personnel. Cross-functional teams facilitate knowledge sharing and practical design decisions.

Use of DFMA Tools and Software

Modern DFMA software tools enable designers to analyze assembly time, cost implications, and manufacturability metrics. These tools provide quantitative feedback that supports informed decision-making.

Training and Organizational Support

Training engineers and technicians in DFMA principles is essential for successful adoption. Management commitment and organizational support further enhance DFMA integration.

Challenges in DFMA Adoption

Despite its benefits, DFMA implementation may face challenges such as resistance to change, lack of DFMA expertise, and limited access to appropriate tools. In some cases, existing production constraints may limit design flexibility. Overcoming these challenges requires organizational commitment, continuous training, and incremental implementation strategies (Tan, 2022).

DFMA and Future Trends in Production Facilities

With the advancement of Industry 4.0, DFMA is increasingly integrated with digital manufacturing technologies such as computer-aided design (CAD), simulation, and additive manufacturing. The use of digital twins and data analytics enhances DFMA effectiveness by enabling real-time evaluation of design decisions. As production facilities move toward smart manufacturing systems, DFMA will continue to play a vital role in optimizing efficiency and competitiveness (Rankohi et al., 2022).

CONCLUSION

Integrating Design for Manufacturing and Assembly (DFMA) in production facilities offers significant benefits, including cost reduction, improved productivity, enhanced quality, reduced time-to-market, and sustainable manufacturing practices. By aligning product design with manufacturing and assembly capabilities, DFMA enables production facilities to achieve operational excellence and maintain competitiveness in an evolving industrial landscape. The successful implementation of DFMA requires early design integration, cross-functional collaboration, and organizational commitment, making it a strategic tool for modern production systems.

REFERENCE

Bao, Y., Favi, C., & Gao, M. (2022). *Design-for-Manufacturing-and-Assembly (DfMA) and Design-for-Deconstruction (DfD) in the construction industry: Challenges, trends and developments. Buildings, 13*(5), Article 1164. https://doi.org/10.3390/buildings13051164 MDPI

Design for Manufacturing and Assembly (DfMA) in Construction: A Holistic Review of Current Trends and Future Directions. (2024). *Buildings, 14*(1), Article 285. https://doi.org/10.3390/buildings14010285 MDPI

Design for manufacturing and assembly methods in the product development process of mechanical products: A systematic literature review. (2022). *The International Journal of Advanced Manufacturing Technology, 120*, 4307–4334. https://doi.org/10.1007/s00170-022-08837-6 Springer

Integrating Design for Manufacture and Assembly (DfMA) with BIM: *Systematic review of drivers and barriers to DfMA-BIM integration.* (2024). *Automation in Construction.* https://doi.org/10.1016/j.autcon.2024.

Lu, W., Tan, Y., & Gao, M. (2020). *Application and benefits of DfMA in industrialized building systems and off-site construction. Journal of Industrialized Construction.* Retrieved from https://www.tandfonline.com/doi/abs/10.1080/24751448.2023.2246804 Taylor & Francis Online

Montazeri, S., Rankohi, S., Carbone, C., & Iordanova, I. (2022). *Design for Manufacturing and Assembly (DfMA) and associated challenges: A multidisciplinary analysis. Espace ETS Research Repository.* Retrieved from https://espace.etsmtl.ca/id/eprint/3462/1/MONTAZERI_Sadaf.pdf Espace ETS

Odo, N., Montazeri, S., Lei, Z., Dewinter, K., & Shokouhy, A. H. (2024). *Integrated framework and impact assessment of DFMA in modular home manufacturing facilities: A case study. Transforming Construction with Off-site Methods and Technologies (TCOT).* https://doi.org/10.57922/49gbba90 Ilmu Data Journal

Rankohi, S., Carbone, C., & Iordanova, I. (2022). *Design-for-Manufacturing-and-Assembly (DfMA) for the construction industry: Review of productivity impacts. Journal of Industrialized*

Construction. Retrieved from https://journalofindustrializedconstruction.com/index.php/mocs/article/download/255/221/464 journalofindustrializedconstruction.com

Razak, M. A. (2022). *DfMA and off-site methods in building delivery: Standardization effects on productivity and waste reduction. Buildings.* https://doi.org/10.3390/buildings15010103 MDPI

Soh, J., Li, X., & Yazdi, N. (2021). *Advances in DFMA-based assembly techniques to improve manufacturing efficiency. International Journal of Production Research.* https://doi.org/10.1080/00207543.2021.

Tan, Y. (2022). *Digital-enabled design for manufacture and assembly (DfMA) in prefabricated production systems. UCL Discovery.* Retrieved from https://discovery.ucl.ac.uk/10154601/2/Tan_2022DfMA.pdf UCL Discovery

Wasim, A., Lu, W., & Gao, M. (2020). *Quantifying benefits and challenges of DFMA in industrial production workflows. Automation in Construction.* https://doi.org/10.1016/j.autcon.2020.103XXXXX (placeholder DOI — see publisher) Espace ETS

Wuni, I. Y. (2020). *DFMA and quality improvement in product lifecycle design: A systematic perspective. Journal of Engineering Design & Technology.* https://doi.org/10.1108/JEDT-06-2020-0189 Espace ETS

Yin, X., Qi, L., & Yuan, J. (2019). *Reducing project duration through DFMA-based modular production: Evidence from industrialized building. Journal of Construction Engineering and Management.* https://doi.org/10.1061/(ASCE)CO.1943-7862.0001661

CHAPTER 3
A SMART AUTONOMOUS ROBOTIC SYSTEM FOR AUTOMATED SURVEILLANCE AND PUBLIC SPACE PROTECTION: AN IORT APPROACH FOR ENHANCED SECURITY[1]

Ivan SUKIN[2]
Anatoly TSIRLIN[3]

[1]This work was funded by the Russian Science Foundation (RSF) under Grant No. 25-29-00965.
[2]ivsukin@gmail.com, ORCID ID: 0000-0002-9861-5796
[3]tsirlin@sarc.botik.ru, ORCID ID: 0000-0002-3637-6160

INTRODUCTION

Conceptual design of heat exchanger networks is often reduced to the MILP kind of problem, which is computationally very hard. To solve such a problem, one must introduce various simplifying assumptions and this often leads to solutions that are only suboptimal. Besides, parameters such as prices are often a subject of a rapid change. For a broad class of thermodynamic processes: heat engines, refrigerators, separation systems are among them, – it is fruitful to use the thermodynamic estimates of efficiency (in the class of irreversible processes, i.e., when the fluxes are infinitesimal). For processes of the heat transfer these estimates make no sense, as the concept of the heat transfer with zero fluxes makes no sense.

It is impossible to estimate the thermodynamic perfection of heat transfer systems without taking into account the boundedness of a contact surface area – the integral heat transfer coefficient and the given heat load – the total amount of heat transferred from hot streams to the cold ones per unit time. The notion of exergy is often used to estimate the thermodynamic perfection of such systems (\cite {Brodjnskiy, Boshnjkovish} etc.). In this case systems are compared by the total losses of available energy (exergy).

Using the exergy analysis framework, one calculates the entropy generation within the system as a function of known heat capacities of streams and their respective temperatures at inlets and outlets of the apparatus. The problem of conceptual design is not existing in this case, so questions like “What are conditions of the minimum entropy generation within the system under some given constraints?” remain unanswered. Current chapter presents answers to these questions. Heat transfer processes are very diverse; they may include streams with various hydrodynamics and different kinetics may govern the process of exchanging of energy between these streams. The matter involved may be presented in various states or phases and even be a subject of a phase transition. Our work shows that the entropy generation of a two-flow heat exchanger has the minimum value for given values of the heat transfer coefficient and heat load. This value is attained in a counter-current tubular heat exchanger, when the ratio of heat capacities of the hot and the cold stream respectively is equal to the inverse ratio of absolute temperatures of these streams and these ratios are constant along the length of the heat exchanger.

We show that for a given heat load (given heat transfer coefficient) the minimum of a heat transfer coefficient (maximum of a heat load) is attained on the curve where an entropy generation is minimal. We obtained the estimate of the minimal entropy generation in a multi-flow heat transfer system and conditions under which this estimate can be attained. The "ideal system" may serve as a reference for a real system that could be driven to the ideality by the choice of its free parameters.

The minimum value of an entropy generation:

- Shows how various parameters (temperatures, heat capacities, heat load, heat transfer coefficient, etc.) affect capabilities of a system.
- Allows one to estimate the thermodynamic efficiency of a working heat transfer system by comparing its actual entropy generation with the attainable minimum value.
- Allows one to plot the boundary of the reachable set of a system. If the design process requirements are such that the entropy generation in the actual system should be less than the calculated minimum value, such system cannot be physically implemented just like a heat engine that has efficiency higher than Carnot efficiency.

We will call streams that have given temperatures and heat capacities as "the given ones" and those whose parameters should be calculated using conditions of minimum entropy generation as "the controlled ones". We need, under specific constraints laid upon the given streams, to choose parameters of the controlled streams in a way minimizing the entropy generation. We present the algorithm of design of a multi-flow heat transfer system with real constraints. The algorithm allows to calculate the number of two-flow heat exchangers to construct the system from, heat loads and heat transfer coefficients for each of these heat exchangers and to choose the structure of the whole system in terms of contacts between streams.

The conditions of the minimum entropy generations are true even when heat capacities are varied, so they give a possibility to consider systems in which some of streams are evaporating or condensing. These conditions allowed us to transform a multi-flow heat transfer system to a thermodynamically equivalent system with two virtual streams.

Computations for this system are much easier and this simplification was used for a design of multi-flow systems.

Mathematical Model of Two-Flow Heat Exchanger and Entropy Generation Minimization

Since heat exchange systems do not transform one substance into another, the system of thermodynamic balances does not contain material balance equations and is reduced to energy and entropy balance equations. Let us consider mathematical models for different interaction organizations, limiting ourselves to steady-state heat exchange, in which the temperatures of the contacting flows change along the contacting surface.

Ideal displacement

The temperature of the cold flow along the length of the heat exchanger changes according to the equation [1]:

$$\frac{dT_-}{dl} = k(l) \cdot \frac{z(T_+, T_-)}{W_-}, \qquad T_-(0) = T_-^{in}, \qquad T_-(L) = T_-^{in} + \frac{\bar{Q}}{W_-} = T_-^{out}. \quad (1)$$

Here W is the heat capacity of the cold flow, equal to the product of its flow rate g_- and the specific heat capacity c_-; z is the heat transfer law that determines the kinetics of heat exchange, k is the specific heat transfer coefficient proportional to the contact surface, Q is the total heat load in [W].

The heat transfer law has the following properties:

$$z(T_+, T_-) \geq 0, \qquad \frac{\partial z}{\partial T_+} > 0, \qquad \frac{\partial z}{\partial T_-} < 0, \qquad z(T_+, T_-) = 0 \Leftrightarrow T_+ = T_-. \quad (2)$$

For definiteness, here and below we will assume that the flow rates are measured in [mol/sec], the heat capacity of substances – in [J/mol K], the heat capacity of flows $W = g$ in [W/K]. The units of k and z depend on the form of kinetics, but their product has the unit [W/m]. Thus, for kinetics linear with respect to the temperature difference (Newtonian) $z = T_+ - T_-$, and the coefficient k has the unit [W/m K].

With constant heat capacity, the entropy production due to a change in the temperature of a cold flow is:

$$\sigma_- = W_- \ln \frac{T_-^{out}}{T_-^{in}} \geq 0. \quad (3)$$

Previous equations could be written for the hot flow similarly:

$$\frac{dT_+}{dl} = -k(l) \cdot \frac{z(T_+, T_-)}{W_+}, \qquad T_+(0) = T_+^{in}, \qquad T_+(L) = T_+^{in} - \frac{\bar{Q}}{W_+} = T_+^{out}. \quad (4)$$

Entropy production due to a change in the temperature of a hot flow is negative (the total entropy production is always positive though):

$$\sigma_+ = W_+ \ln \frac{T_+^{out}}{T_+^{in}} < 0. \quad (5)$$

If a flow changes its phase state, the entropy production associated with this process is:

$$\sigma_r = \frac{g \cdot r}{T_b}, \quad (6)$$

where g is the flow rate, r is the latent heat of phase transition, and T_b is the temperature at which the phase transition occurs. The quantity σ_r is positive if the flow evaporates and negative if it condenses.

The total entropy production in a two-flow heat exchanger, if no phase transitions occur in it, is equal to:

$$\sigma = \sigma_+ + \sigma_- = W_+ \ln \frac{T_+^{out}}{T_+^{in}} + W_- \ln \frac{T_-^{out}}{T_-^{in}} > 0. \quad (7)$$

We will denote cumulative values of the heat flow, entropy generation and heat transfer coefficient on the interval from $l = 0$ to some $l = l'$ as $Q(l')$, $\sigma(l')$ and $K(l')$ respectively. The change in these variables is characterized by equations

$$\begin{gathered} \frac{dQ}{dl} = k(l) \cdot z(T_+, T_-), \qquad Q(0) = 0, \qquad Q(L) = \bar{Q}; \\ \frac{d\sigma}{dl} = k(l) \cdot z(T_+, T_-) \left(\frac{1}{T_-} - \frac{1}{T_+} \right), \qquad \sigma(0) = 0; \\ \frac{dK}{dl} = k(l), \qquad K(0) = 0, \qquad K(L) = \bar{K}. \end{gathered} \quad (8)$$

Ideal mixing

Let a flow (the cold one for definiteness) enter a mixing chamber, where its temperature is uniform and equal to the temperature at the outlet of the heat exchanger. Entropy generation due to a change in the parameters of this flow consists of two components: mixing of the incoming flow with temperature T_-^{in} with what is in the tank and has temperature T_-^{out}, and an increase in entropy due to the heat received.

Similarly, for a hot flow, the change in entropy consists of the entropy of mixing, which is always positive, and a decrease in entropy due to heat transfer.

Entropy production during mixing of two flows with temperatures T_1, T_2 and heat capacities W_1, W_2 is equal to the sum of the entropy production associated with each of them:

$$\sigma_-^m = W_1 \ln\frac{T^{out}}{T_1} + W_2 \ln\frac{T^{out}}{T_2}, \qquad T^{out} = \frac{W_1T_1 + W_2T_2}{W_1 + W_2}. \tag{9}$$

Ideal mixing for one of the flows corresponds to the model when it mixes with an infinitely large recirculating flow entering the same chamber. In this case, the heat capacity of one of the flows in the formula (9) tends to infinity. For definiteness, let it be W_2, and W_1 — the heat capacity of the flow entering the mixer. Let us find the limit σ_-^m when the heat capacity W_2 tends to infinity.

Using L'Hôpital's rule, we obtain:

$$\sigma_-^m = W_1\left(\frac{T_1}{T_2} - 1 - \ln\frac{T_1}{T_2}\right). \tag{10}$$

This expression is always positive if the temperature of the incoming flow differs from the temperature of the flow in the mixer. If the flow in the mixing mode is cold, then its heat capacity and temperature

are equal to W_-, T_-^{in}, and taking into account the increase in its entropy due to the receipt of heat, we obtain:

$$\sigma_-^m = W_-\left(\frac{T_-^{in}}{T_-^{out}} - 1 - \ln\frac{T_-^{in}}{T_-^{out}}\right) + \frac{\bar{Q}}{T_-^{out}}, \qquad T_-^{out} = T_-^{in} + \frac{\bar{Q}}{W_-}. \tag{11}$$

After replacing $\bar{Q} = W_-\left(T_-^{out} - T_-^{in}\right)$ and substituting into equality (11), we obtain

$$\sigma_-^m = W_- \ln\frac{T_-^{out}}{T_-^{in}}. \tag{12}$$

Therefore, *the total entropy production due to the change in flow temperature in the ideal mixing regime coincides with the entropy production for the flow in the displacement regime.*

If the hot flow is in the mixing regime, then similarly:

$$\sigma_+^m = W_+\left(\frac{T_+^{in}}{T_+^{out}} - 1 - \ln\frac{T_+^{in}}{T_+^{out}}\right) - \frac{\bar{Q}}{T_+^{out}}, \qquad T_+^{out} = T_+^{in} - \frac{\bar{Q}}{W_+}. \tag{13}$$

After eliminating the heat load $\bar{Q}$ through the temperatures and heat capacity of the hot flow, we obtain similarly to how this was done for the cold flow

$$\sigma_+^m = W_+ \ln \frac{T_+^{out}}{T_+^{in}}, \tag{14}$$

which coincides with the result obtained for the displacement mode.

Statement: Entropy production is determined by the expression (7). It depends only on the heat capacities of the flows, their temperatures at the inlet and outlet of the heat exchanger, associated with the heat load, and does not depend on the kinetics of heat exchange and the hydrodynamics of the flows.

In this case, the heat transfer coefficient K depends on the hydrodynamics

of the flows and the kinetics of heat exchange.

Simplification of the model using transition to the new independent variable

The presented model with ideal displacement can be simplified significantly by transitioning to a new independent variable that monotonously depends on l. The most suitable variable for this is the heat load $Q(l)$. After replacing l with Q, taking into account the equations (8), we obtain the system

$$\frac{dT_+}{dQ} = -\frac{1}{W_+(T_+)}, \qquad T_+(0) = T_+^{in}, \qquad T_+\left(\overline{Q}\right) = T_+^{out}; \tag{15}$$

$$\frac{dT_-}{dQ} = \frac{1}{W_-(T_-)}, \qquad T_-(0) = T_-^{in}, \qquad T_-\left(\overline{Q}\right) = T_-^{out}; \tag{16}$$

$$\frac{d\sigma}{dQ} = \frac{1}{T_-(Q)} - \frac{1}{T_+(Q)}, \qquad \sigma(0) = 0. \tag{17}$$

For constant heat capacities

$$T_-(Q) = T_-^{in} + \frac{Q}{W_-}, \quad T_+(Q) = T_+^{in} - \frac{Q}{W_+}.$$

The entropy production in a heat exchanger for any flow hydrodynamics, including displacement with co-current flow, is equal to

$$\sigma\left(\overline{Q}\right) = W_- \ln \frac{T_-\left(\overline{Q}\right)}{T_-^{in}} + W_+ \ln \frac{T_+\left(\overline{Q}\right)}{T_+^{in}}. \tag{18}$$

For the heat transfer coefficient, we obtain

$$\frac{dK}{dQ} = \frac{1}{z\left(T_+(Q), T_-(Q)\right)}, \qquad K(0) = 0, \qquad K\left(\overline{Q}\right) = \overline{K}. \tag{19}$$

Note that the temperature dependences on the heat load are determined only by the heat capacities of the flows. To derive the above-mentioned dependences, we need to know these heat capacities and take into account one of the boundary conditions for each temperature. For constant heat capacities of the flows, the temperatures are affine functions of Q. The kinetics (temperature multiplier z) is included only in the equation for the heat transfer coefficient. Dependencies (15)–(18) are valid for any heat exchange kinetics.

Countercurrent flow

With a counter-current flow arrangement of a heat exchanger, one of the flows (hot, to be specific) enters the heat exchanger in section L and exits in section zero. This leads to a change in the sign of dl and dQ. As a result, equation (15) takes the form

$$\frac{dT_+}{dQ} = \frac{1}{W_+(T_+)}, \qquad T_+\left(\overline{Q}\right) = T_+^{in}, \qquad T_+(0) = T_+^{out}. \tag{20}$$

For a constant heat capacity, we have

$$T_+(Q) = T_+^{in} - \frac{\overline{Q} - Q}{W_+}. \tag{21}$$

Since heat capacities of the flows are always positive, in the case of counterflow, the slopes of the dependences between temperatures and the heat load will be positive for both flows.

Phase State Change

If a hot flow enters a heat exchanger in the form of steam and partially or completely condenses within it, then for calculations it is convenient to represent this flow as two flows, one of which is completely condensed, and the second is a liquid flow with a given heat capacity. Similarly, for a partially evaporating liquid, it is necessary to distinguish the flow of completely evaporating and the flow of heated liquid. Therefore, we will give formulas for the flow of completely condensing steam and completely evaporating liquid. It is necessary to know their boiling temperatures T_b in [K], flow rate in g [kg/sec], heat of vaporization/condensation r in [J/kg].

The entropy production associated with the condensation of a hot flow or the boiling of a cold flow is

$$\sigma_{kn} = -\frac{gr}{T_b}, \quad \sigma_{kp} = \frac{gr}{T_b}.$$

When the phase state changes, the heat capacity of the flow tends to infinity, so the slope of the dependence $T(Q)$ at the value of Q equal to the heat flux released during the phase transition is zero. It is also zero when the flow passes through an ideal mixing heat exchanger, but in this case the dependence of its temperature on Q experiences a jump to the temperature at the outlet of the mixing chamber and remains constant at the value of Q equal to the heat load of this heat exchanger (Fig. 1).

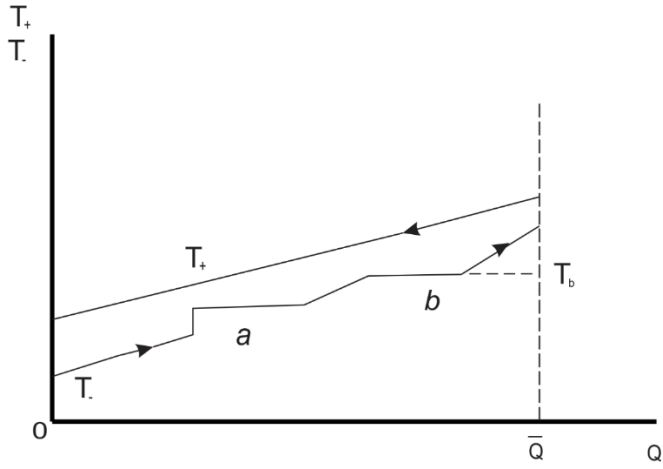

Figure 1. Difference Between Dependences of Flow Temperatures on Heat Load (For A Cold Flow (A) Is the Ideal Mixing Zone, (B) Is the Boiling Zone)

Ideal Heat Transfer System

Reachable set of two-flow heat exchange

The thermodynamic indicators characterizing the heat exchange process are $\overline{Q}$, σ, $\overline{K}$. In the works [2, 3] it is shown that for given values of $\overline{Q}$ and $\overline{K}$ the value of σ in any two-flow heat exchanger is bounded from below. This limitation isolates the reachable set in the space of thermodynamic indicators. The shape of the boundary of the reachable set depends on the type of the kinetic equation and is determined by the solution of the problem:

$$\sigma = \int_0^{\overline{Q}} \left(\frac{1}{T_-(Q)} - \frac{1}{T_+(Q)} \right) dQ \to \min_{T_-(Q), T_+(Q)} \tag{22}$$

given the constraint:

$$\int_0^{\overline{Q}} \frac{dQ}{z\left(T_+(Q), T_-(Q)\right)} = \overline{K}. \tag{23}$$

Let us present the solution of this problem. The optimality condition (minimum dissipation condition) has the form:

$$\frac{z\left(T_+(Q), T_-(Q)\right)}{T_-(Q)\sqrt{-\frac{\partial z}{\partial T_-}}} = \frac{1}{\overline{K}} \int_0^{\overline{Q}} \frac{dQ}{T_-(Q)\sqrt{-\frac{\partial z}{\partial T_-}}} = const. \tag{24}$$

Since $\frac{\partial T_-}{\partial Q} = \frac{1}{W_-(Q)}$, then, knowing this dependence, we can find the law of change of the heat capacity of the corresponding cold flow.

If the law of change in the temperature of the cold flow is given, then for the temperature of the hot flow, minimizing irreversibility, we obtain a similar equation:

$$\frac{z\left(T_+(Q), T_-(Q)\right)}{T_+(Q)\sqrt{\frac{\partial z}{\partial T_+}}} = \frac{1}{\overline{K}} \int_0^{\overline{Q}} \frac{dQ}{T_+(Q)\sqrt{\frac{\partial z}{\partial T_+}}} = const. \tag{25}$$

For most types of kinetics, these equations can only be solved numerically.

Let us concretize the condition (24) for the case, when the temperature factor has the form

$$z = (T_+^n - T_-^n).$$

We obtain:

$$\frac{|T_+^n - T_-^n|}{\sqrt{T_-^{n+1}}} = \frac{1}{\overline{K}} \int_0^{\overline{Q}} \frac{dQ}{\sqrt{T_-^{n+1}}} = const. \tag{26}$$

Newtonian kinetics ($n = 1$), counter-current thermodynamically consistent heat exchanger

For $n = 1$, equation (24) may be solved analytically, and this leads to the requirement of constancy of the flow temperature ratio for any value of Q, which allows constructing the boundaries of heat exchange feasibility in the space of thermodynamic indicators.

In the minimum dissipation mode for counter-current heat exchange:

$$\frac{T_-(Q)}{T_+(Q)} = m = 1 + \frac{\sigma_+}{\overline{K}} = \frac{W_+}{W_-} = \frac{T_-^{in} + \dfrac{\overline{Q}}{W_-}}{T_+^{in}}. \qquad (27)$$

Here $\sigma_+(\overline{Q}) = W_+ \ln \frac{T_+^{in} - \overline{Q}/W_+}{T_+^{in}}$ is a monotonic function of $\overline{Q}$, which is the change in entropy associated with the hot flow (it is negative). The unit of this quantity is [W/K]. The heat capacities of the flows are assumed to be constant.

The conditions of minimum dissipation (27) are satisfied in a countercurrent flow heat exchanger if each flow is in the ideal displacement mode, and the ratio of the heat capacities of the flows is inverse to the ratio of their temperatures in any cross-section (*the heat capacity of the hot flow is as many times less than the heat capacity of the cold flow as the temperature of the hot flow is greater than the temperature of the cold flow*). They are called the ***conditions of thermodynamic consistency of heat transfer***.

The value of the minimum dissipation in accordance with (22) is

$$\sigma^* = -W_+ \left(\frac{1}{m} - 1\right) \ln \frac{T_+^{out}}{T_+^{in}} = -\left(\frac{1}{m} - 1\right) \sigma_+(\overline{Q}). \qquad (28)$$

From conditions (20), (27) it follows that

$$m = 1 + \frac{\sigma_+}{\overline{K}}, \quad \sigma^* = \frac{\sigma_+^2}{\overline{K} + \sigma_+}. \qquad (29)$$

For a fixed heat load $\overline{Q}$, the expression (28) defines the boundary of the reachable set of two-flow heat exchange in the plane “heat transfer coefficient “— “entropy generation”. The greater the heat load, the further this boundary moves from the origin. The heat transfer coefficient *K* reaches its minimum on this boundary.

Relations (27) allow us to find the dependence of the minimum possible heat transfer coefficient of a two-flow heat exchanger on the heat load. This dependence has the form:

$$\overline{K}^*(\overline{Q}) = -\frac{W_+ T_+^{in}}{T_+^{in} - T_-^{in} + \dfrac{\overline{Q}}{W_-}} \ln \frac{T_+^{in} W_+ - \overline{Q}}{W_+ T_+^{in}}. \qquad (30)$$

Thus, the problem of minimum irreversibility for a given heat load and heat transfer coefficient and the problem of minimum heat transfer coefficient for given temperatures of inlet flows, their heat capacities and the heat load (i.e., given some entropy generation value) are dual to each other and have the same solution.

If for some heat exchanger K and $\overline{Q}$ are such that the point A corresponding to them is inside the reachable set, then by organizing the process close to thermodynamically consistent counter-current heat exchange, it is possible to either increase the heat load or decrease the heat transfer coefficient, reaching the feasibility boundary.

Formulas for two-flow heat exchangers with different hydrodynamic modes

The expression (18) for calculating the irreversibility factor in a two-flow heat exchanger was obtained above. It defines the relationship between an entropy generation and a heat load for any combination of hydrodynamic modes of the contacting flows:

- Mixing-mixing.
- Mixing-displacement.
- Displacement-displacement (cocurrent, countercurrent).

The dependence of the heat transfer coefficient on the heat load is different for each type of kinetics and each combination of flow hydrodynamics. Sometimes the heat load is specified, in other cases it must be found for a given heat transfer coefficient. In Table. 1 for Newtonian kinetics, expressions are given for the heat transfer coefficient depending on the thermal load and the thermal load depending on $\overline{K}$ and the heat capacities of the flows for various combinations of their hydrodynamic types.

In the Table 1 it is designated:

$$A = \frac{W_- - W_+}{W_+ W_-}, \quad B = \frac{W_- + W_+}{W_+ W_-}.$$

If in a counter-current heat exchanger the displacement heat capacities of the flows are the same $W_- = W_+ = W$, the heat transfer coefficient

$$\overline{K} = \frac{\overline{Q}}{T_+^{in} - T_-^{in} - \frac{\overline{Q}}{W}}, \quad \overline{Q} = \frac{W(T_+^{in} - T_-^{in})\overline{K}}{W + \overline{K}}.$$

Table 1. Thermodynamic Indicators of Two-Flow Heat Exchangers.

Hydrodynamic mode	$\overline{Q}$	$\overline{K}$
Mixing-mixing	$\overline{K}(T_+^{out} - T_-^{out})$	$\frac{\overline{Q}}{T_+^{out} - T_-^{out}}$ $T_+^{in} - T_-^{in} > B\overline{Q}$
Displacement-displacement (cocurrent)	$\frac{1}{B}(T_+^{in} - T_-^{in})(1 - e^{-\overline{K}B})$	$\frac{1}{B}\ln\frac{T_+^{in} - T_-^{in}}{T_+^{in} - T_-^{in} - B\overline{Q}}$
Mixing (cold) – displacement (hot)	$W_+(T_+^{in} - T_-^{out})(1 - e^{-\frac{\overline{K}}{W_+}})$	$W_+\ln\frac{T_+^{in} - T_-^{out}}{T_+^{in} - T_-^{out} - \overline{Q}/W_+}$
Mixing (hot) – displacement (cold)	$W_-(T_+^{out} - T_-^{in})(1 - e^{-\frac{\overline{K}}{W_-}})$	$W_-\ln\frac{T_+^{out} - T_-^{in}}{T_+^{out} - T_-^{in} - \overline{Q}/W_-}$
Displacement-displacement (countercurrent)	$\frac{1}{A}(T_+^{out} - T_-^{in})(e^{\overline{K}A} - 1)$	$\frac{1}{A}\ln\frac{T_+^{out} - T_-^{in} + A\overline{Q}}{T_+^{out} - T_-^{in}}$

The ratio of entropy production $\overline{\sigma}^*$ for an ideal heat exchanger to entropy production $\overline{\sigma} = \sigma_+ + \sigma_-$ in a heat exchanger with the same heat transfer coefficient and heat load can serve as an indicator of the thermodynamic efficiency of the process $0 \le \eta \le 1$.

To go from the heat transfer coefficient to the heat exchange surface, it is necessary to know the specific heat transfer coefficient per unit contact area. It should also be taken into account that when the phase state changes, the specific heat transfer coefficient increases sharply (by 4–5 times) and depends on the boiling mode (nucleate or film).

Flow Evaporation/Condensation

Next, we consider the problem of estimating the entropy generation and the relationship between the heat transfer coefficient and the heat load for the case where one or both contacting flows change their phase state. In this case, we assume that the heat load is Q [W], the boiling/condensation temperature is T_b [K], the flow rate is g [kg/sec], the specific heat capacities of the liquid and steamare C_f, C_p [J/kg·K], the heat of vaporization/condensation is r [J/kg], the mass fraction of liquid in wet steam $0 \le d \le 1$ are known.

We will initially consider the case where the hot flow enters the heat exchanger in the form of superheated steam with a temperature $T_+^{in} > T_b$. It goes through three stages:

- Cooling to the boiling point.
- Partial or complete condensation.
- Cooling of the condensate, if the heat load is large enough.

Let us write down the expression for the entropy generation associated with the change in the state of the hot flow for each of these stages (it is always negative):

1. Steam cooling stage

$$\sigma_{+I} = W_{+I}\ln\frac{T_b}{T_+^{in}}, \quad Q_I = W_{+p}\left(T_+^{in} - T_b\right).$$

Here $W_{+p} = g_+ C_p$.

2. Condensation stage

$$\sigma_{+II} = -\frac{g_+ r}{T_b}, \quad Q_{II} = g_+ r.$$

3. Liquid cooling stage

$$\sigma_{+III} = W_{+III}\ln\frac{T_b - \frac{Q_{III}}{W_{+f}}}{T_b}.$$

Here $W_{+f} = g_+ C_f, \quad Q_{III} = Q - Q_I - Q_{II}$.

The total entropy production associated with the hot flow, $\sigma_+ = \sigma_{+I} + \sigma_{+II} + \sigma_{+III}$.

For a cold flow receiving heat Q and entering the heat exchanger with temperature $T_-^{in} < T_b$, the entropy production by stages is equal to:

1. Liquid heating stage

$$\sigma_{-I} = W_{-f}\ln\frac{T_b}{T_-^{in}}, \quad Q_I = W_{-f}(T_b - T_-^{in}).$$

Here $W_{-f} = g_- C_f$.

2. Boiling stage

$$\sigma_{-II} = \frac{g_- r}{T_b}, \quad Q_{II} = g_- r.$$

3. Steam superheating stage

$$\sigma_{-III} = W_{-p}\ln\frac{T_b + Q_{III}/W_{-p}}{T_b}.$$

Here $W_{-p} = g_{-}C_p, \quad Q_{III} = Q - Q_I - Q_{II}$.

All terms of entropy production associated with the change in the state of the cold flow $\sigma_{-} = \sigma_{-I} + \sigma_{-II} + \sigma_{-III}$ are positive and their sum in absolute value exceeds σ_{+}.

In the case when the hot flow enters the system at the boiling temperature in the form of wet steam, the proportion of liquid in which is equal to d, it goes through only two stages of condensation and cooling of the steam. In this case, at the condensation stage

$$Q_{II} = g_{+}(1-d)r, \sigma_{+II} = -\frac{Q_{II}}{T_b}.$$

The same applies to the case when the cold flow enters in the form of wet steam. It goes through only the stages of evaporation of the liquid and heating of the steam. At the evaporation stage

$$Q_{II} = g_{-}dr, \sigma_{-II} = \frac{Q_{II}}{T_b}.$$

Calculation of the heat transfer coefficient

To calculate the heat transfer coefficient when the phase state of the flow changes, it is necessary to know the kinetics of heat exchange and the hydrodynamics of the contacting flow. For Newtonian kinetics, you can use the formulas contained in Table 1. Initially, the heat transfer coefficients are calculated for each of the three/two stages of changing the parameters of the flow changing the phase state, taking into account the heat load at each of the stages. At the boiling/condensation stages, the temperature of this flow is uniform and its hydrodynamics can be considered identical to the hydrodynamics of ideal mixing, substituting the boiling/condensation temperature T_b into the formulas for calculating K instead of the outlet temperature of the flow. The total heat transfer coefficient is equal to the sum of the coefficients calculated for each stage.

Constant heat flow direction condition

For any value of the heat load Q, the condition of constant heat flow sign must be satisfied. Due to the properties of the kinetic function, it comes down to the fact that the difference $\Delta(Q) = T_{+}(Q) - T_{-}(Q)$ must be positive for $0 \leq Q \leq \overline{Q}$. We will write these conditions first for constant and then for variable heat capacities of flows.

For constant heat capacities

$$\Delta(Q) = T_+(Q) - T_-(Q) = T_+^{in} - T_-^{in} - \frac{\overline{Q}}{W_+} + Q\left(\frac{1}{W} \pm \frac{1}{W_-}\right) > 0. \quad (31)$$

This expression is linearly dependent on Q, therefore, in order for it to be satisfied for any thermal load, it is sufficient that it be satisfied for that of its extreme values at which the term dependent on Q is minimal. This minimum is

$$Q^0 = 0, \text{if } W_+ \le W_-; \quad Q^0 = \overline{Q} \quad \text{if} \quad W_+ > W_-. \quad (32)$$

Thus, the condition of constancy of the sign of q imposes a limitation on the heat load of the heat exchanger

$$\overline{Q} < \left(T_+^{in} - T_-^{in}\right)\min(W_+, W_-). \quad (33)$$

For varied heat capacities

$$\Delta(Q) = T_+(Q) - T_-(Q) =$$
$$\left(T_+^{in} - T_-^{in}\right) - \left[\int_Q^{\overline{Q}} \frac{dQ}{W_+(Q)} + \int_0^Q \frac{dQ}{W_-(Q)}\right] > 0. \quad (34)$$

In this expression, only the term enclosed in square brackets depends on Q. Let us denote it by $F(Q)$. For the sign constancy condition to be satisfied, the inequality $\max_Q F(Q) < (T_+^{in} - T_-^{in})$ must be satisfied. The maximum of this function can be achieved either at the extreme points $Q = 0, Q = \overline{Q}$, or at the stationary point $F(Q)$. It is easy to show that the stationary point is the root of the equation $W_+(Q) - W_-(Q) = 0$.

If one of the flows evaporates or condenses, then its heat capacity changes abruptly, and the function $F(Q)$ experiences a kink. Its maximum can be achieved at the kink point if the heat capacity of the flow before this point is less than after. For a cold flow, this is the point of the onset of boiling, and for a hot flow, this is the point of the onset of condensation.

Since the function $F(Q)$ consists of two terms, the first of which decreases monotonically with the growth of Q, and the second monotonically increases, then the stationarity point Q^0 is unique.

Therefore, we have the constraint

$$\max\left(F(0); F\left(\overline{Q}\right); F(Q^0)\right) < \left(T_+^{in} - T_-^{in}\right). \quad (35)$$

Conceptual Design of Multiflow Heat Transfer Systems

Reachability limits of a heat exchange system, we will first consider a multi-flow heat exchange system with minimal constraints. We will assume that only the system heat load $\overline{Q}$, the total heat transfer coefficient $\overline{K}$, which indirectly characterizes the total contact surface, the input temperatures, and the heat capacities of hot or cold flows, are given. Further, for definiteness, we will assume that the parameters of hot flows are given.

We the problem of the limiting capabilities of such a system ("ideal" multiflow heat exchange). There the minimum possible entropy generation σ^* was found, it was shown that for the case when the heat flux is proportional to the temperature difference (Newtonian kinetics), the entropy production is bounded from below and this bound can be reached if:

- At each contact point, the ratio of absolute temperatures of the flows $\frac{T_-}{T_+} = m$ is the same for all heat exchangers in the system.
- The temperatures of the flows at the outlet of the system are the same for all hot and all cold flows.
- Each two-flow cell must be a counter-current, thermodynamically consistent displacement heat exchanger.

When these requirements are met, the minimum possible entropy generation at fixed temperatures and heat capacities W_i of the hot flows are related to their temperatures at the inlet T_i^{in} and the total heat transfer coefficient $\overline{K}$ as:

$$\left.\begin{aligned} m &= 1 - \frac{1}{\overline{K}} \sum_{i=1}^{n} W_{+i} \left(\ln T_{+i}^{in} - \ln T_{+}^{out}\right), \\ \overline{\sigma}^* &= \overline{K} \frac{(1-m)^2}{m}. \end{aligned}\right\} \tag{36}$$

The temperature of the hot flows at the outlet, as follows from the energy balance conditions, is equal to:

$$T_{+}^{out} = \frac{\sum_{i=1}^{k} T_{+i}^{in} W_{+i} - \overline{Q}}{\sum_{i=1}^{k} W_{+i}}, \tag{37}$$

It is not advisable to use hot flows with initial temperatures lower than T_{+}^{out} in the heat exchange system.

If part of the hot flows condenses during the heat exchange process, then in the expression (36) for m the heat capacity of the corresponding term tends to infinity. Let us assign the index "k" to the condensing flow and find the limit $W_{+k}(\ln T_k^{in} - \ln T_+^{out}) = W_{+k}\left(\ln T_k^{in} - \ln(T_k^{in} - \frac{Q_k}{W_{+k}})\right)$ as W_k tends to infinity. Using L'Hôpital's rule to resolve uncertainties, we find that

$$\lim_{W_{+k}\to\infty} W_{+k}\left(\ln T_k^{in} - \ln(T_k^{in} - \frac{Q_k}{W_{+k}})\right) = \frac{Q_k}{T_k^{in}} = \frac{g_k r_k}{T_{bk}}.$$

Here we have taken into account that the temperature T_k^{in} is equal to the condensation temperature T_{bk}, and the heat load is equal to the product of the flow rate and the latent heat of vaporization.

Thus, the expression for m in the presence of condensing flows is rewritten in the form:

$$m = 1 - \frac{1}{K}\left(\sum_{i\neq k} W_{+i}\left(\ln T_i^{in} - \ln T_+^{out}\right) + \sum_k \frac{g_k r_k}{T_{bk}}\right). \quad (38)$$

The dependence of the minimum possible irreversibility on the heat transfer coefficient (the limit of thermodynamic feasibility of the heat exchange system) at a fixed heat load has the same form (28) as for two-flow heat exchange, with the difference that

$$\sigma_+ = \sum_{i\neq k} W_{+i}\left(\ln T_i^{in} - \ln T_+^{out}\right) + \sum_k \frac{g_k r_k}{T_{bk}}. \quad (39)$$

We will call flows for which input temperatures and heat capacities are specified *fixed ones*. In the case where cold flows are fixed, expressions (37) and (38) will take the form

$$T_-^{out} = \frac{\sum_{i=1}^{k} T_{-i}^{in} W_{-i} + \overline{Q}}{\sum_{i=1}^{k} W_{-i}}, \quad (40)$$

$$m = 1 - \frac{1}{K}\left(\sum_{i\neq k} W_{-i}\left(\ln T_-^{out} - \ln T_{-i}^{in}\right) + \sum_k \frac{g_k r_k}{T_{bk}}\right). \quad (41)$$

In a more general case, a part of hot and a part of cold flows can be fixed. In this case, the system can be divided into two subsystems, the thermal conductivity coefficient and entropy production will be equal to the sum of these indicators found for each. The heat load between the subsystems must be distributed so that the ratio m of the cold temperature to the hot is the same for both subsystems.

For any deviation from the conditions of minimum dissipation, the point corresponding to the parameters of the heat exchange system $\overline{K}$, $\overline{Q}$ deviates upward from the boundary of the reachable set.

Implementation of an Ideal System. Equivalent Two-Flow Heat Exchanger

An ideal system with fixed hot flows can be implemented as a system of parallel two-flow heat exchangers with displacement-displacement counter-current flow hydrodynamics, the number of which is equal to the number of hot flows. The conditions of minimum dissipation determine the parameters of the cold flows. They must have the same temperature at the inlet $T_{-}^{in} = mT_{+}^{out}$, the heat capacity of each flow must be equal to $W_{-i} = W_{+i}/m$. The heat load of each of these heat exchangers $Q_i = \frac{T_{+i}^{in} - T_{+i}^{0ut}}{W_{+i}}$, which together with the heat capacity determines the temperature of the cold flow at the outlet. If a hot flow condenses, then the cold flow in contact with it must evaporate at a boiling temperature of $T_{b-} = mT_{b+}$.

Statement: *There is a two-flow heat exchanger, each of the flows in which changes its heat capacity with a change in temperature, such that its thermodynamic parameters: heat load, heat transfer coefficient, entropy production are the same as those of a multi-flow system.* We will call this heat exchanger equivalent to the system.

In such a heat exchanger, equivalent hot and cold flows contact in a counter-flow mode with displacement. We will construct the dependence of the temperatures of these flows on the heat load in the counter-current flow regime, and then for a more general case we will show that its thermodynamic parameters are the same as those of a multi-flow system. We will denote by Q the heat flow transferred to the cold flow when it is heated to $T_{-}(Q)$. Then, with counter-current flow, the heat given off by the hot flow is equal to $Q_{+} = \overline{Q} - Q$.

- Hot flow. We require that for any current heat load $0 \le Q \le \overline{Q}$ and the corresponding temperature $T_{+}(Q)$ of the equivalent hot flow, the heat capacity of the equivalent flow is equal to the sum of the heat capacities of the hot flow of the system having this temperature.

This means that for $Q = \overline{Q}$ and temperature T_+^{out}, the heat capacity of the equivalent flow is equal to the total heat capacity of all hot flow $W_+ = \sum_i W_{+i}$. The slope of the dependence $T_+(Q)$ is minimal. We arrange the hot flows by their inlet temperatures so that $T_{+i}^{in} > T_{+(i+1)}^{in}$. Then the slope of the equivalent temperature will be minimal until it reaches the lowest of the inlet temperatures of the hot flows T_{+k}^{in}. At this point, the number of hot flows participating in heat exchange decreases and the slope becomes equal to $\frac{1}{\sum_{i=1}^{k-1} W_{+i}}$. The next break occurs at a temperature equal to the temperature at the inlet of the $(k-1)$-th flow, etc. At $Q = 0$, the slope of the $T_+(Q)$ dependence is equal to $1/W_{+1}$.

- Cold flow. We require that for any current heat load $0 \le Q \le \overline{Q}$ and the corresponding temperature $T_-(Q)$ of the equivalent cold flow, the heat capacity of the equivalent flow is equal to the sum of the heat capacities of the cold flows of the system that have this temperature.

The dependence $T_-(Q)$ is constructed in the same way as for the hot flow, with the difference that in the counter-current flow, the value $Q = \overline{Q}$ for the hot one corresponds to $Q = 0$ for the cold one. Since for each of the cold flows the heat capacity is equal to the heat capacity of the corresponding hot one, divided by m, and their values at the output are m times less than the input temperatures of the hot flows, then $T_-(Q) = mT_+(Q)$, which corresponds to the condition of minimum dissipation. The curves of equivalent temperatures are monotonic and convex downwards (Fig. 2).

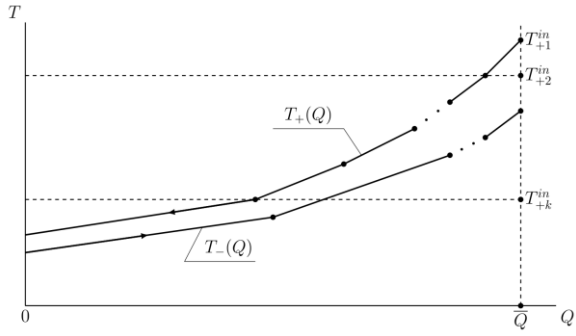

Figure 2. Dependence of Equivalent Flow Temperatures on Heat Load For an Ideal System

If the fixed flows are cold, then the construction of $T_{-}(Q)$ and then $T_{+}(Q)$ is completely analogous.

In real heat exchange systems, the restrictions on the flow parameters usually differ from those listed above for an ideal system. The flow temperature can be fixed at the inlet and outlet of the system, the heat capacities can be determined not exactly, but in a certain range, it is usually not possible to ensure contact between the evaporating and condensing flows with a given ratio of their boiling/condensation temperatures, etc.

The ability to build a two-flow heat exchanger equivalent to a real multi-flow system is very important, since it allows you to choose the free parameters of the system so that the dependences of the temperatures of equivalent flows are as close as possible to such dependences for a heat exchanger equivalent to an ideal system.

Algorithm For Synthesis of Heat Exchange System

In real multi-flow heat exchange systems integrated with the technological process, restrictions on flow parameters do not allow to accurately fulfill the conditions of minimum dissipation. Some flow parameters, free parameters, may not be fixed or lie within specified limits. Conditions of ideal heat exchange and temperature dependences for a heat exchanger equivalent to an ideal system can serve only as a “guiding light” when choosing these parameters. And the value of entropy production in an ideal system is similar to the Carnot efficiency for heat engines. Below we present an algorithm for synthesis of multi-flow systems based on these considerations. The value of the ratio $\overline{\sigma}^{*}$ to entropy production in the designed system is an indicator of its thermodynamic quality.

Thermodynamic Equivalence of Heat Exchange Systems

Definition: *Two heat exchange systems are thermodynamically equivalent if the values of the thermodynamic quality indicators:* $\overline{Q}, \sigma, \overline{K}$ *are the same for them.*

When designing a system integrated with a process, the temperatures of some of the flows at the input and output of the system, their heat capacities and the heat load $\overline{Q}$ are specified.

It is necessary to select the contact structure, heat transfer coefficients (heat exchange surfaces), heat loads and heat capacities (flow rates) of the flows for two-flow cells. We will a priori assume that for each cell, as well as for an equivalent heat exchanger, the counter-current flow conditions are valid:

$$\frac{dT_+}{dQ}\frac{dT_-}{dQ} \geq 0, \tag{42}$$

where $T_+(Q)$, $T_-(Q)$ are the temperatures of the equivalent flows.

System synthesis algorithm:

- Plot the dependencies of the hot and cold flows in a two-flow heat exchanger equivalent to the designed system on the current heat load.
- Select "homogeneity intervals" for the constructed dependencies $T_+(Q), T_-(Q)$, on each of which the slopes of both these dependencies do not change.
- "Improve" the equivalent heat exchanger indicators by choosing free flow parameters.
- Evaluate the thermodynamic quality of the equivalent heat exchanger.
- Select the contact structure, heat loads and heat transfer coefficients of the two-flow cells.

Construction of "initial" flow temperature dependencies on the heat load in an equivalent heat exchanger

We fix the free flow parameters at some average permissible values and, for fixed inlet and outlet temperatures and given heat capacities, we construct the temperature dependencies of equivalent flows on the heat load Q in the same way as was done for an ideal system. Then we show that a heat exchanger with flows and their heat capacities $W_+(Q) = \frac{dT_+}{dQ}$, $W_-(Q) = \frac{dT_-}{dQ}$ selected in this way is thermodynamically equivalent to a multi-flow system in accordance with the definition given above.

Hot flow. We construct it so that for each value of temperature and corresponding heat load of the equivalent hot flow, its heat capacity is equal to the total heat capacity of hot flow having the given temperature. To do this:

- We arrange the hot flow of the multi-flow system by their input temperature so that $T_{+1}^{in} > T_{+2}^{in} > T_{+3}^{in} > \cdots$ and construct the dependence $T_+(Q)$, starting with $Q_+ = 0$, $Q = \overline{Q}$.

- For $Q = \overline{Q}$ the value of T_- is equal to the highest of the hot flow temperatures at the input to the system T_{+1}^{in}, and the heat capacity determining the slope in the first interval is equal to W_{1+}. The first interval ends when the temperature T_+ becomes equal to T_{+2}^{in}.
- In the second interval, the second flow "joins" the first one and the heat capacity becomes equal to $W_{+1} + W_{+2}$ (the slope of the curve decreases). The interval ends either when the temperature of the combined flow reaches the temperature T_{-3}^{in}, or when it becomes equal to the temperature of the outlet of one of the two hot flows from the system. In the first case, the third flow "joins" and the total heat capacity increases, in the second case, in the next, third, interval, the heat capacity will be equal to the total heat capacity of the hot flows remaining in the system.
- This procedure continues until the temperature $T_+(Q)$ reaches the lowest temperature of the cold flows at the inlet to the system or the heat load becomes equal to $\overline{Q}$.

Cold flow. We arrange the cold flows by their temperature at the inlet of the system so that $T_{-1}^{in} < T_{-2}^{in} < T_{-3}^{in} < \cdots$ and construct the temperature $T_-(Q)$, starting from $Q = 0$ to $\overline{Q}$:

- At $Q = 0$, the temperature $T_-(Q) = T_{-1}^{in}$, and the heat capacity of the equivalent flow in the first interval is equal to the heat capacity of the first of the cold flows.
- The first interval of constant heat capacity of the cold flow ends when the temperature $T_-(Q)$ is equal to T_{-2}^{in}. At this point, the second flow "joins" the first flow, and the heat capacity of the equivalent flow in the second interval becomes equal to the total heat capacity of the first two.
- The second interval ends either when the temperature of the combined flow reaches the temperature T_{-3}^{in}, or when this temperature becomes equal to the temperature of the first or second cold flows leaving the system. In the first case, the third flow "joins" and the heat capacity increases, in the second case, at the next third interval, the heat capacity will be equal to the total heat capacity of the flows remaining in the system.

- This construction continues until $Q = \overline{Q}$. If $T_+(\overline{Q}) > T_-(\overline{Q})$, then the system is realizable and hot flows with $T_{+i}^{in} < T_+(0)$ should be excluded from the system. If $T_+(0) < T_-(0)$, then the system is not realizable and hot flows should be added to it.

Note that the calculation of each of the temperatures of the equivalent flows occurs independently and is determined only by the boundary temperatures and heat capacities of the hot and cold flows of the system. Each exit from the system or inclusion of a heat carrier flow, as well as evaporation or condensation of one of the flows on the constructed curves corresponds to a break point.

The heat capacity of each of the equivalent flows for any heat load (or temperature that monotonously depends on a heat load) is equal to the total heat capacity of the flows included in the equivalent cold and hot flows for a given heat load. If the equivalent flow includes a flow that changes its phase state, then in the evaporation/condensation section the temperature of the equivalent flow is constant and equal to the boiling point.

We will call the interval of heat load values the homogeneity interval if the heat capacities of both equivalent flows are constant on this interval. There are no break points on this interval on either the upper or lower curve.

Statement: *The two-flow heat exchanger obtained using this construction is thermodynamically equivalent to a multi-flow system.*

Indeed, the value of the total flow of transferred heat $Q = \overline{Q}$ in a multi-flow system is determined by the total change in the enthalpy of the cold flows. And it coincides with the value $Q = \overline{Q}$ in the equivalent two-flow heat exchanger, since at each interval the supplied heat flow in the equivalent heat exchanger is equal to the sum of the heat flows supplied in this range of change of Q from hot to cold flows of the multi-flow system.

The entropy generation in the equivalent heat exchanger

$$\bar{\sigma} = \int_0^{\bar{Q}} \left(\frac{1}{T_-(Q)} - \frac{1}{T_+(Q)} \right) dQ \qquad (43)$$

also coincides with the production of entropy in a multi-flow system, since the temperatures of the flows at each interval of change of Q coincide with the temperatures of the flows in a multi-flow system.

Finally, the heat transfer coefficient of the equivalent heat exchanger

$$\overline{K} = \int_0^{\overline{Q}} \frac{dQ}{z(T_-(Q), T_+(Q)} \tag{44}$$

is equal to the total heat transfer coefficient of the multi-flow system due to the equality of temperatures of the contacting flows for each value of Q. In this case, at each interval of change in the heat load, the temperature multiplier $z(T_+, T_-)$ can have a different form.

This proves the equivalence of the two-flow heat exchanger for a multi-flow system with the selected flow parameters.

The fact that the two-flow heat exchanger is thermodynamically equivalent to a multi-flow system allows, when synthesizing the system, to select the free variables of the system so as to optimize the thermodynamic indicators of the equivalent heat exchanger (to bring it closer to a thermodynamically consistent counter-current flow heat exchanger corresponding to an ideal system). After this, it is necessary to find such a structure of contacts and the distribution of heat transfer coefficients between the two-flow cells of the system that would correspond to it.

Calculation of the number of two-flow heat exchangers

The dependences of the temperatures of equivalent flows on Q determine the total number of two-flow heat exchangers N in the system. To find it, we introduce the concept of a *passthrough pair* of flows of order ν.

Definition: *A passthrough pair of flows of order ν is a combination of hot and cold flows whose heat capacities are included as terms in the heat capacities of equivalent flows on ν adjacent homogeneity intervals.* We denote the number of such pairs as $n^{\nu}, \nu \geq 2$. A passthrough pair corresponds to one instead of ν two-flow heat exchangers.

Let n_+^{μ} hot and n_+^{μ} cold flows contact on each μ-th homogeneity interval. The maximum of these two numbers is denoted as n_*^{μ}, and the difference as Δn^{μ}. If $\Delta n^{\mu} > 0$, then some of the cold streams should branch, and if this difference is less than zero, then the hot ones' branch.

The total number of two-stream heat exchangers in the system is:

$$N = \sum_{\mu=1}^{M} n_*^{\mu} - \sum_{\nu=2}^{M} n_{\nu}\,(\nu - 1).$$

Here n_ν is the number of passthrough pairs of order ν, M is the total number of homogeneity intervals. For some values of ν it can be equal to zero.

"Improvement" of an equivalent heat exchanger by choosing free parameters

The objectives of "improvement" of an equivalent heat exchanger are to choose the free parameters to

- Reduce the number of homogeneity intervals and increase the number and the order of passthrough pairs, and hence to reduce the number of two-flow heat exchangers in the designed system.
- Reduce entropy production in the equivalent heat exchanger, and hence in the designed system, by approaching the ideal one.

The number of homogeneity intervals decreases if the projections of the breakpoints of the curves $T_+(Q)$ and $T_-(Q)$ on the abscissa axis coincide. Therefore, if the boundary temperature of the hot flow is free, it should be chosen so that the breakpoint of the equivalent temperature of the hot dlow shifts and its abscissa coincides with the abscissa of the nearest breakpoint of the equivalent cold flow. The same applies to the free boundary temperature of the cold flow.

A reduction in the number of two-flow cells with a minimal increase in irreversibility can be realized by increasing the order of passthrough pairs if the heat capacities of the flows in adjacent intervals differ little from each other and can be made equal. A passthrough pair must have the maximum order. If different combinations of flows can be selected for its formation with the same order, then it is advisable to select one for which the ratio of absolute temperatures and the ratio of heat capacities exactly or approximately satisfy the conditions of thermodynamic consistency (27).

An increase in the flow rate decreases the slope of the corresponding dependence of the equivalent temperature on the heat load and extends the homogeneity interval. For example, in Fig. 4 the fourth homogeneity interval corresponds to a very small increase in the heat load and it can be combined with the third or fifth interval with an increase in the flow rate of the cold flow in the third or with an increase in the flow rate of the hot flow in the fifth interval.

To reduce entropy production, it is necessary to choose free values of the heat capacities of the flows so that the ratio of equivalent temperatures $T_-(Q)/T_+(Q)$ for any value of Q approaches a constant. An increase in the heat capacity of the hot flow increases this ratio, an increase in the heat capacity of the cold flow decreases it. To bring this ratio closer to a constant, it is necessary to calculate $m(Q) = T_-(Q)/T_+(Q)$ and the average value of this indicator $\overline{m}$ for the equivalent heat exchanger constructed at the preliminary stage. In those sections where the temperature ratio is above average, reduce the heat capacity of the equivalent hot flow and increase the heat capacity of the cold flow, and in the section where $m(Q) < \overline{m}$, change the free heat capacities of the flows in the opposite direction.

In some cases, the choice of free parameters reduces both dissipation and the number of homogeneity intervals.

For example, let the total heat flow $\overline{Q}_1$ be given in the first interval of heating the cold flow, leaving the system hot. It is necessary to distribute these heat loads between parallel heat exchangers so that the entropy production in the system is minimal. This corresponds to the requirement that the entropy flow leaving the system together with the hot flows

$$\sigma_+^{out} = \sum_j W_j \ln(T_{+j}^{in} - Q_j/W_{+j})$$

be maximal provided that $\sum_j Q_j = \overline{Q}_1$. The optimality conditions for this problem, obtained from the requirement of stationarity with respect to Q_j of the corresponding Lagrange function, lead to the requirement of equality of temperatures of all hot flows at the system outlet. The projections of the outlet temperatures on the abscissa axis are the same, which reduces the number of homogeneity intervals.

Therefore, *If the temperatures of all or part of the hot flows at the outlet are free, then in the optimal case they should be chosen to be the same*.

Similar considerations lead to the requirement of equality of free temperatures at the outlet for cold flows.

Note that the plotting of temperatures in the same coordinates is performed in the “pinch analysis” [4-6] based on heuristic considerations. In this case, they strive to keep the difference, and not the ratio, of the flow temperatures constant.

Synthesis of a multi-flow system using an "improved" equivalent heat exchanger

Due to technological limitations, the flows can be separated or merged. When separating flows, their heat capacities must be selected so that the temperature increases are the same.

When synthesizing a multi-flow system equivalent to a two-flow heat exchanger, the following conditions must be met:

- The temperatures of the flows at the inlet to each two-flow heat exchange cell corresponding to the ν-th homogeneity interval must be equal to $T_{+\nu}^{in}$, $T_{-\nu}^{in}$.
- The ratio of the heat capacities of the cold and hot flows in each heat exchange cell corresponding to the ν-th homogeneity interval must be equal to the ratio of the heat capacities of the equivalent flows $\frac{W_-}{W_+}$ on this interval.

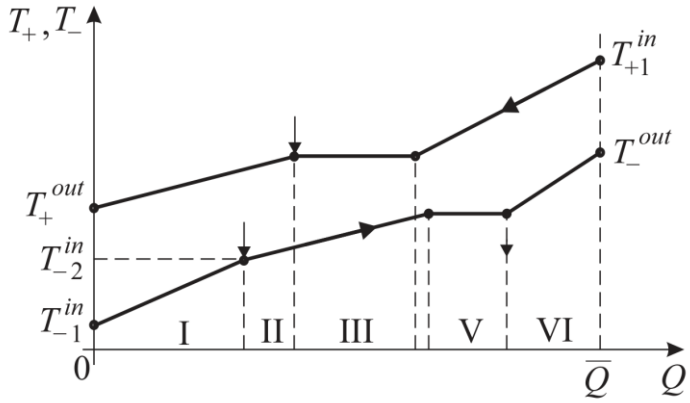

Figure 3. Dependences Of Equivalent Flow Temperatures on The Heat Load (The Homogeneity Intervals Are Numbered with Roman Numerals).

These *equivalence conditions* allow us to construct a multi-flow system in the following sequence:

- Select passthrough pairs of flows and find the total number of multi-flow cells using formula (45). Such selection does not change the boundaries of the homogeneity intervals and the value of Δn^{μ}.

Only n_*^{μ} decreases, and therefore the number of two-flow heat exchangers corresponding to the μ-th interval.

- On the first homogeneity interval, for each of the cold flows, the temperature at the inlet to the cell of the hot flow in contact with it and its flow rate (heat capacity) are determined from the second equivalence condition. The heat load for each of the two-flow heat exchange cells is found as the product of the heat capacity of any of the flows by the difference in its temperatures. Knowing the heat capacities and temperatures of the contacting flows allows us to calculate the heat transfer coefficient of the cell with known heat transfer kinetics using the formulas given in Table 1.
- Repeat the same procedure for the second homogeneity interval, etc. In this way, we obtain the structure, distribution of heat loads and heat transfer coefficients for a multi-flow system. In this case, it is almost always advisable for each hot flow to contact several cold ones and vice versa.

Evaluation of Thermodynamic Quality

Based on the heat capacities and temperatures of the flows at the input and output of the resulting system, the total entropy production is calculated as the sum of the products of the heat capacity of each flow and the logarithm of the ratio of its temperature at the output to its temperature at the input to the system and compared with the entropy production in an ideal heat exchange system with the same heat load and total heat transfer coefficient.

CONCLUSION

In this chapter expressions for calculating heat transfer coefficient for a given heat load and boundary parameters of flows in two-flow heat exchangers with different hydrodynamics were presented. Three indicators of thermodynamic quality of multi-flow heat exchange systems are introduced: heat load, total heat transfer coefficient and entropy production. It is shown that for given values of the first two, entropy production (dissipation) is bounded from below.

Conditions for such organization of heat exchange that corresponds to the minimum of dissipation are presented, and it is shown the boundary corresponding to the minimum of dissipation is the Pareto set for the remaining two indices. We show that entropy generation in a two-flow heat exchanger depends only on the heat capacities of the flows and their boundary temperatures and does not depend on the kinetics of heat exchange and the hydrodynamics of the flows. The concept of thermodynamic equivalence of heat exchange systems is introduced. An algorithm for constructing the dependences of flow temperatures on the heat load in a two-flow heat exchanger equivalent to a multi-flow heat exchange system is presented. A formula is obtained for calculating the total number of two-flow heat exchangers in a multi-flow system based on the type of temperature curves of equivalent flows. An algorithm for synthesis of multi-flow systems based on the concept of thermodynamic equivalence is proposed.

REFERENCES

Andresen, B., & Gordon, J. M. (1992). Optimal heating and cooling strategies for heat exchanger design. *Journal of Applied Physics*, *71*(1), 76–79. https://doi.org/10.1063/1.350649.

Kemp, I. C. (2007). *Pinch analysis and process integration: a user guide on process integration for the efficient use of energy*. Elsevier.

Linnhoff, B., & Hindmarsh, E. (1983). The pinch design method for heat exchanger networks. *Chemical Engineering Science*, *38*(5), 745–763. https://doi.org/10.1016/0009-2509(83)80185-7.

Prigogine, I. (1968). *Introduction to Thermodynamics of Irreversible Processes*. John Wiley & Sons.

Smith, R. (2005). *Chemical process design and integration*. Wiley.

Sukin, I. A., Balunov, A. I., & Tsirlin, A.M. (2021). *Approaches of irreversible thermodynamics in the problems of conceptual design of separation and heat transfer processes (Metody neobratimoj termodinamiki v zadachakh sinteza system teploobmena I razdelenija).* Russian Academy of Sciences. *(in Russian)*

Tsirlin, A. M. (2017). Ideal Heat Exchange System. *Journal of Engineering Physics and Thermophysics*, *90*(5), 1035–1042. https://doi.org/10.1007/s10891-017-1654-2.

CHAPTER 4
CONSTITUTIVE MODEL FOR AXIAL FREQUENCY WITH STRAIN GRADIENT THEORY OF CYLINDRICAL SHELLS

Muzamal HUSSAIN[1]

[1]Department of Physical and Numerical Sciences, University of Rasul 50370, Mandi Bahauddin, Pakistan, muzamal.hussain@putrasul.edu.pk, ORCID ID: 0000-0002-6226-359X

INTRODUCTION

Materials classified as functionally graded (FGMs) are those whose formation and function can fluctuate over time. FGMs are inhomogeneous, meaning that their characteristics vary with time, and they are now being used non hot environments. The frequencies of composite cylindrical shells containing fluid were calculated by Sharma et al. (1998). They used trigonometric functions to estimate the axial modal deformations.

Di Taranto and Lessen (1964) studied the infinitely long spinning cylindrical shells for vibration that are thin and isotropic. Using the Rayleigh-Ritz formulation, Sharma (1974) examined the vibration frequencies of a circular cylinder and compared his findings with a few experimental ones. The frequency response of fluid-filled CSs was examined by Chung et al. (1981), who also provided an analysis of experimental and analytical research. Generalized end conditions were used by Penzes and Kraus (1972) to examine the vibrations of rotating cylindrical shells. Due to the requirement for an approximate method and calculation procedure, the analysis of rotating shells was limited to a few exceptional circumstances.

Advanced computers have completely transformed shell vibration analysis with their potent numerical approaches. In 2007, Najafizadeh and Isvandzibaei established their study on the FG material properties. Ergin and Temarel (2002) investigated cylindrical shell vibration. The horizontally oriented shells were submerged in the fluid they held. Donnell's shallow-shell model was applied to the quiescent, dense, incompressible, and inviscid fluid by Amabili et al. (1999). Collection of the nonlocal continuum models was created by (Ghavanloo *et al.* 2019) and associates in order to investigate the nanoparticles' vibratory breathing mode.

Within different research, created an innovative depending on size general beams theory as an examine of static deformation of curved nanobeams' both in and out of the air behavior within the framework of a nonlocal differential-based model. The bending that is not linear study of orthotropic annular/circular graphene sheets with several layers was examined by (Dastjerdi and Jabbarzadeh, 2017).

Şimşek (2011) investigated the aspect ratio's impacts, stiffness of medium, in addition to the nonlocal parameter on the natural frequencies and provided a critical formula regarding the simple-supported double-orthotropic nonlocal nanoplates implanted in an elastic medium and their nonlocal frequencies (Rahmani et al. 2017). Additionally, the impact of the shell's interior and external sides is examined in the dense fluid. The vibration frequencies of composited spinning cylindrical shells were compared, and the outcomes were assessed using various shell theories. Furthermore, due to the fact that the classical continuity technique does not have scale independence, it cannot account for size effects that result from working at small scales. Despite the fact that the traditional theory of continuity is occasionally used as an examine the way nanostructures behave mechanically, like carbon nanotubes, it is discovered to be insufficient due to its disregard for size effects (Abazari *et al.* 2015). Using sigmoid law distribution and the hygrothermal impact, Pankaj et al. (2019) investigated the functionally graded material. Aspect ratio frequency spectra have been illustrated based on different edge situations. To characterize three-dimensional structures and to describe the local mechanical behavior, classical elastic shell model was developed. This model was widely applied in MTs modeling to study the radical pressure and buckling modes of MTs under uniform external axial compressive forces (Gao *et al.* 2010). Li and Lam (1998) studied influence of edge conditions vibration frequencies and modes of rotating composite CSs. In their study of the differential quadrature (DQ) approach in structural mechanics, Bert and Malik (1996) resolved an eight-order coupled differential equation problem and contrasted the outcomes of the (DQ) solution with the shell's natural frequencies. While there are now many advanced tools available due to the stress examination of complex frameworks, such beam models, the finite element approach, are still commonly used in pre-design because they offer important insights through the behavior of constructions (Kaufmann *et al*. 2020). Since experimentally characterizing nanotubes can be challenging, and computational atomistic simulations can be time-consuming, continuous models have been used to frequently employed as an examine vibrational actions of CNT-based mass sensors (Natsuki and Natsuki, 2023).

Farahani and Barati (2015) studied vibration investigation of shell which is inundated in the incompressible fluid and by seeing axial and lateral hydrostatic pressure Flugge shell equation is used and the equation from which method it is recognized is wave propagation. Yang and Lim (2011) created an analytical model of a nonlocal cylindrical shell to examine the Propagation of axisymmetric waves in carbon nanotubes. Golpayegani and Ghorbani (2016) described the free vibrations of the thin cylindrical shell of FGM, the effects of non-uniform internal pressure on free vibrations, and the effects of various parameters on natural frequencies. They explained the vibrational properties of a revolving cylindrical shell made of functionally graded material. In this paper, effect of different parameters are investigated with strain gradient theory. Applications of coupled nanobeams include mass sensors and biosensors nanobeam resonators both nano-optical and nano-actuators. Both double and multiple nanobeam systems (DNBS and MNBS) are complex systems made up of two or more parallel nanobeams coupled by a Van der Waals force, elastic media, or forces resulting from nano-optical phenomena (Ahmadi, 2022).

In this chapter, stress and strain gradient theory (Askes and Aifantis, 2011) has been used to discuss the mechanical property i.e. wave propagation of orthotropic cylindrical shell considering cylindrical shell model and the size parameters in stress strain gradient elasticity theory and also use love's thin shell theory and few basic laws such as, Hook's law and the Hamilton principal.

As a result, in this study, the vibration behavior of cylindrical shell is assessed using a stress strain gradient theory. The stress-strain relationship was first expressed originally for axisymmetric waves to check the frequency analysis of cylindrical shells with circumferential wave number, length- and height to radius ratios. Therefore, this investigation gives one of the fundamental concepts about the cylindrical shells which have a number of considerable applications in industries.

1. MATERIAL AND METHODS

The modeled problem is converted into an algebraic system of equations by using the wave propagation solution, and these equations can then be solved for specific situations. A graphic discussion of the size parameter's impact is also included.

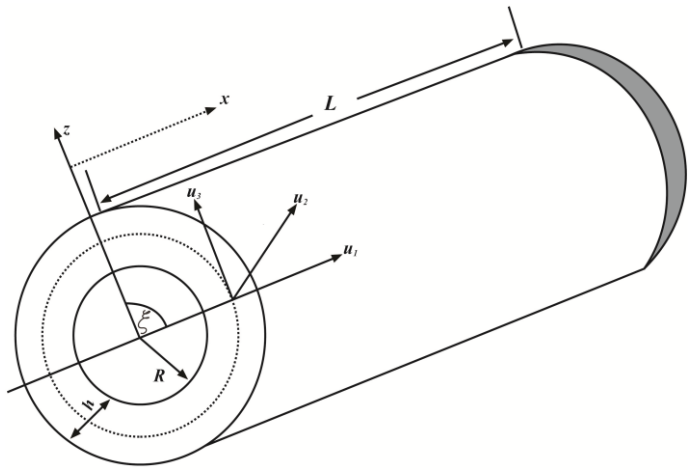

Figure 1. Cylindrical Shell Model

A structure that is compatible with the structure of shells and is represented by the cylindrical shell model is taken into consideration. In an orthotropic scenario, nine independent parameters three Young moduli, three Shear moduli, and three Poisson's coefficients are needed to examine the mechanical behavior of a cylindrical shell in the three primary directions. For thin shell and plane stress, it will come down to four parameters in this instance. Here, the parameters are denoted as Longitudinal modulus (E_x), circumferential modulus (E_ξ), shear modulus of shell $\left(G_{x\xi}\right)$, Poisson's ratio in axial direction $\left(\Upsilon_{x\xi}\right)$, Poisson's ratio in axial direction $\left(\Upsilon_{\xi x}\right)$, equivalent thickness (H); effective thickness for bending (h_o), medium radius of shell (R), mass density per unit volume (ρ).

1.1 Stress Strain Gradient Elasticity Theory

Stress strain gradient theory is the result of combining Erigen's stress gradient theory with strain gradient theory. The strain energy density determines the stress strain gradient elasticity theory, which is represented as follows:

$$\Xi = \frac{1}{2}\int_{\forall} \gamma_{ij}\lambda_{ij}\, d \tag{1}$$

The strain energy density Ξ, stress components γ_{ij}, and strain components λ_{ij} are all included in the equation above.

$$(1-\mu_d^2\Theta^2)\gamma_{ij} = D_{ijkl}(1-\mu_s^2\,\Theta^2)\lambda_{kl} \tag{2}$$

The size parameter for the static and dynamic instances, respectively, is represented by μ_s and μ_d and in the aforementioned Equation (2), where Θ^2 is the Laplacian operator and is a stiffness matrix. In both static and dynamic cases, the size parameters' values are not equal but rather rely on the size of the representative volume element (Lam et al., 2003; Fleck et al., 1994). The components of displacements u_1, u_2, u_3 in axial, radial, and circumferential directions are shown in Fig. 1, which is the schematic representation of the cylindrical shell model. The values of the displacement vectors in the cylindrical shell can be expressed as follows using Love's thin shell theory:

$$u_1(x,\xi,z,t) = u_1'(x,\xi,t) - z\frac{\partial u_3'}{\partial x}$$

$$u_2(x,\xi,z,t) = u_2'(x,\xi,t) - \frac{z}{R}\left(\frac{\partial u_3'}{\partial \xi} - u'\right)$$

$$u_3 = u_3'(x,\xi,t) \tag{3}$$

The displacements $u_1'(x,\xi,t)$, $u_2'(x,\xi,t)$, $u_3'(x,\xi,t)$ of the shell's main plate are shown in Eq. (3) above. The classical strain can now be represented using the coordinate axes, displacement vector values provided in Eq. (3), and the assumption of plane strain as follows:

$$\lambda_{xx} = \frac{\partial u_1}{\partial x}$$

$$\lambda_{zz} = \frac{\partial u_3}{\partial z}$$

$$\lambda_{\xi\xi} = \frac{1}{R\left(1+\frac{z}{R}\right)}\left[\frac{\partial u_2}{\partial \xi} + u_3\right]$$

$$\lambda_{xz} = \lambda_{zx} = \frac{1}{2}\left[\frac{\partial u_3}{\partial x} + \frac{\partial u_1}{\partial z}\right]$$

$$\lambda_{x\xi} = \lambda_{\theta x} = \frac{1}{2}\left[\frac{\partial u_2}{\partial x} + \frac{1}{R\left(1+\frac{z}{R}\right)}\frac{\partial u_1}{\partial \xi}\right]$$

$$\lambda_{\xi z} = \lambda_{z,\xi} = \frac{1}{2}\left[\frac{1}{R\left(1+\frac{z}{R}\right)}\frac{\partial u_3}{\partial \xi} + \frac{\partial u_2}{\partial z} + \frac{u_2}{R\left(1+\frac{z}{R}\right)}\right] \quad (4)$$

The following nonzero strain components were produced by applying Love's assumption $(1+z/R) \approx 1$ and entering the values from Eq. (3) into Eq. (4):

$$\lambda_{xx} = \frac{\partial u_1'}{\partial x} - z\frac{\partial^2 u_3'}{\partial x^2}$$

$$\lambda_{\xi\xi} = \frac{1}{R}\frac{\partial u_2'}{\partial \xi} + \frac{u_3'}{R} - \frac{z}{R^2}\frac{\partial^2 u_3'}{\partial \xi^2}$$

$$\lambda_{x\xi} = \lambda_{\xi x} = \frac{1}{2}\left[\frac{1}{R}\frac{\partial u_1'}{\partial \xi} + \frac{\partial u_2'}{\partial x} - \frac{2z}{R}\frac{\partial^2 u_3'}{\partial x \partial \xi}\right] \quad (5)$$

The following form was produced by multiplying Eq. (1) by $(1-\mu_d^2\Theta^2)$ and replacing the nonzero strain components from Eq. (5):

$$(1-\mu_d^2\Theta^2)\Xi = (1-\mu_d^2\Theta^2)\int_\xi \int_x \{\int_{\frac{-h}{2}}^{\frac{h}{2}} [\gamma_x \frac{\partial u_1'}{\partial x} - \gamma_x z \frac{\partial^2 u_3'}{\partial x^2} + \gamma_\xi \frac{\partial u_2'}{R\partial \xi} + \gamma_\xi \frac{u_3'}{R} - \gamma_{\xi z} \frac{\partial^2 w_o}{R^2 \partial \xi^2} + \gamma_{x\xi} \frac{\partial u_1'}{R\partial \xi}$$

$$+\gamma_{x\xi} \frac{\partial u_2'}{\partial x} - 2\gamma_{x\xi} z \frac{\partial^2 u_3'}{R\partial x \partial \xi}]dz\} Rdxd\xi \tag{6}$$

By simplifying Eq. (6) above, we can determine the strain energy for a cylindrical shell, which is as follows:

$$A_1\Xi = \int_\theta \int_x A_1 \begin{bmatrix} N_x \frac{\partial u_1'}{\partial x} - M_x \frac{\partial^2 u_3'}{\partial x^2} + N_\xi \left(\frac{\partial u_2'}{R\partial \xi} + \frac{u_3'}{R} \right) - M_\xi \frac{\partial^2 u_3'}{R^2 \partial \xi^2} \\ \\ +N_{xu_3'} \left(\frac{\partial u_1'}{R\partial \xi} + \frac{2z}{R} \frac{\partial^2 u_3'}{\partial x \partial \xi} \right) - 2M_{xu_3'} \frac{\partial^2 u_3'}{R\partial x \partial \xi} \end{bmatrix} Rdxd\xi \tag{7}$$

where $A_1 = (1-\mu_d^2\Theta^2)$, the expression for kinetic energy in terms of a cylindrical shell can be expressed as follows using Eq. (3):

$$\eta = \frac{1}{2}\rho \int_\xi \int_x \{\int_{\frac{-h}{2}}^{\frac{h}{2}} [(\frac{\partial u_1'}{\partial t} - z\frac{\partial^2 u_3'}{\partial x \partial t})^2 + (\frac{\partial u_2'}{\partial t} - \frac{z}{R}\frac{\partial^2 u_3'}{\partial t \partial \xi})^2 + \left(\frac{\partial u_2'}{\partial t} \right)^2 \Big] dz\} Rdxd\xi \tag{8}$$

The work that external forces produce on a cylindrical shell can be stated as follows:

$$\Gamma = \int_\xi \int_x \left(f_x u_1' + f_\xi u_2' + f_z u_3' \right) Rdxd\xi \tag{9}$$

The cylindrical shell's equation of motion can be found using the definition of the Hamilton principle.

$$\int_{t_1}^{t_2} (\Omega\eta + \Omega\Gamma - \Omega\Xi)dt = 0 \tag{10}$$

By putting the values of η, Γ and Ξ in the form of delta variation in Eq. (10) and multiplying it by $(1-\mu_d^2\Theta^2)$. The final expression of the cylindrical shell's equation of motion, which is based on the stress-strain gradient elasticity theory, is obtained by integrating the resultant equation and setting the coefficients of $\Omega u_1', \Omega u_2', \Omega u_3'$ to zero. This is known as the orthotropic cylindrical shell.

$$A_2\left[a_1\frac{\partial^2 u_1'}{\partial x^2}+a_2\left(\frac{\partial^2 u_2'}{\partial x\partial\xi}+\frac{\partial u_3'}{\partial x}\right)+a_3\frac{\partial^2 u_1'}{\partial\xi^2}+a_4\frac{\partial^2 u_2'}{\partial x\partial\xi}\right]$$
$$=A_1\left(\rho Rh\frac{\partial^2 u_1'}{\partial t^2}\right)-A_1Rf_x \tag{11}$$

$$A_2\left[b_1\frac{\partial^2 u_2'}{\partial x\partial\xi}+b_2\left(\frac{\partial^2 u_2'}{\partial\xi^2}+\frac{\partial u_3'}{\partial\xi}\right)+b_3\frac{\partial^2 u_1'}{\partial x\partial\xi}+b_4\frac{\partial^2 u_2'}{\partial x^2}\right]$$
$$=A_1\left(\rho Rh\frac{\partial^2 u_2'}{\partial t^2}\right)-A_1Rf_\theta \tag{12}$$

$$A_2\left[c_1\frac{\partial^4 u_3'}{\partial x^4}+c_2\frac{\partial^4 u_3'}{\partial x^2\partial\xi^2}+c_3\frac{\partial^4 u_3'}{\partial x^2\partial\xi^2}+c_4\frac{\partial^4 u_3'}{\partial\xi^4}+c_5\frac{\partial^4 u_3'}{\partial x^2\partial\xi^2}+c_6\frac{\partial u_1'}{\partial x}+c_7\left(\frac{\partial u_2'}{\partial\xi}+u_3'\right)\right]$$
$$=A_1\left(\frac{\rho Rh^3}{12}\frac{\partial^4 u_3'}{\partial x^2\partial t^2}+\frac{\rho h^3}{12R}\frac{\partial^4 u_3'}{\partial\xi^2\partial t^2}-\rho Rh\frac{\partial^2 u_3'}{\partial t^2}\right) \tag{13}$$

Where the values of $A_1, A_2, a_1, a_2, a_3, a_4, b_1, b_2, b_3, b_4, c_1, c_1, c_2, c_3, c_4, c_5, c_6, c_7$ are shown in Appendix-I. We will now solve equations (11) through (13) while ignoring the body forces in order to determine the wave propagation of a cylindrical shell. Using displacements and axisymmetric waves, which are determined by the circumferential wave number n = 0, the equation of motion is solved. Let's look at the solution for axisymmetric waves, which is as follows:

$$u_1'(x,t)=\varsigma_1 sin(\delta x-\omega t)$$

$$u_2'(x,t)=\varsigma_2 cos(\delta x-\omega t)$$

$$u_3'(x,t)=\varsigma_3 cos(\delta x-\omega t) \tag{14}$$

The amplitude of longitudinal, circumferential and radial direction is represented by $\{\varsigma_1,\varsigma_2,\varsigma_3\}$. c and δ are the wave velocity and wave vector. The following expressing can be obtaing after substituting the Eq. (14) into Equation. (11) - (13).

$$[-A_2\left(a_1\delta^2\right)+A_1\rho Rh\delta^2\omega^2]\varsigma_1-A_2a_2\delta\varsigma_3=0$$

$$\left[-A_2b_4\delta^2+(A_1\rho Rh\delta^2\omega^2\right]\varsigma_2=0$$

$$A_2c_6\delta\varsigma_1+[A_2(c_1\delta^4+c_7)-A_1\rho Rh\left(\frac{h^2\delta^2c^2}{12}+\delta^2\omega^2\right)]\varsigma_3=0 \tag{15}$$

Now by rewriting the above equations in matrix form we get:

$$\left[L_1-\omega^2A_1\right]\varepsilon_o=0 \tag{16}$$

Where the matrices L_1 and A_1 shows the matrix.

Also $\{\varepsilon_o\}^T=\{\varsigma_1,\varsigma_2,\varsigma_3\}$ and ω is wave velocity. Above equation (29) give non trivial solution if,

$$L_1-\omega^2A_1\varepsilon_o=0 \tag{17}$$

2. RESULTS AND DISCUSSION

In this paper, vibrational frequencies for cylindrical shells are presented and analyzed. In the present model, the stress strain gradient theory is used for the fundamental frequency of cylindrical shell. For the validity of present model, the result are compared with earlier investigation (Xiang, *et al.* 2002; Xuebin, 2008) as shown in the Tables 1~2. The results are well matched with the results of (Xiang, *et al.* 2002; Xuebin, 2008). The percentage difference is negligible and due the required outcomes, it is observed that the stress strain gradient theory is used for the interpretation of frequency analysis.

Table 1. Convergence of SS-SS Frequencies with Frequency Parameter $\lambda=\omega R\sqrt{(1-v^2)\rho/E}$ (Xiang et al. 2002).

n	Method	m		
		1	2	3
1	Xiang et al. (2002)	0.0161029	0.039271	0.1098116
	Present	0.0161028	0.0392714	0.1098115

Table 2. Convergence Of Clamped-Clamped Frequencies with Frequency Parameter $\lambda = \omega R\sqrt{(1-\nu^2)\rho / E}$ (Xuebin, 2008).

Method	n			
	2	3	4	5
Xuebin (2008)	0.014052	0.022726	0.042272	0.068116
Present	0.014256	0.022713	0.042215	0.06805

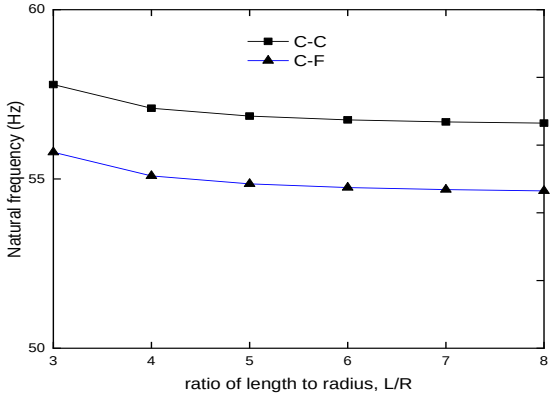

Figure 2. Frequencies Versus *L/R*.

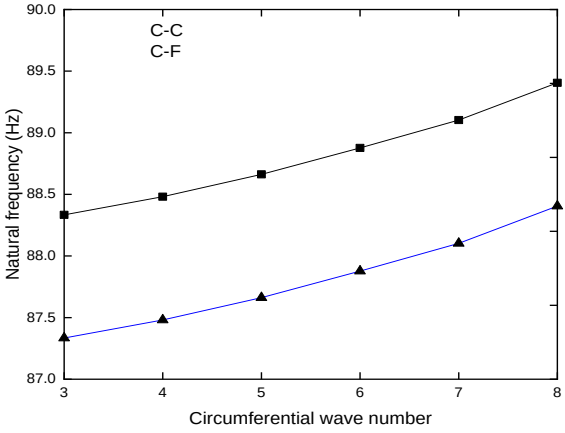

Figure 3. Frequencies Versus Circumferential Wave Number

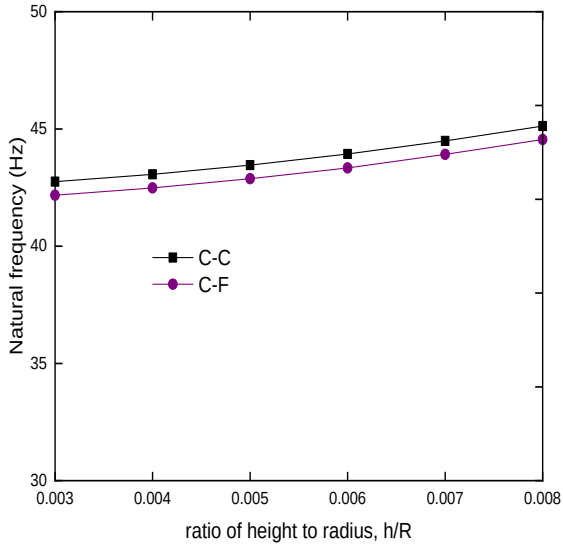

Figure 4. Frequencies Versus h/R.

Here, the graph in Fig. 2 shows the natural frequencies versus length to radius ratio. The frequencies decrease with an increase of length to radius ratio. The frequency behavior is seen with $L/R = 3\sim7$. Also, it is observed that as inner radius is reduced so the fundamental frequencies for all end conditions diminishes. The frequencies of clamped-clamped boundary conditions are greater than that of clamped-free boundary conditions. The decreasing is very fast for the short length ($L/R = 3 \sim 4$) and reduce slowly till the end of the length. The frequencies become parallel from L/R = 5 ~8. Frequencies versus circumferential wave number is shown in the Fig. 3 with two different boundary conditions. The CF attains lowest fundamental frequency as compared to CC. It is observed from the Fig. 3 that the wave number increases as frequencies decreases ranging from $h/R= 3 \sim7$. This analysis uses the stress strain gradient theory. The gap between the frequency curves of clamped-clamped and clamped-free is content throughout the increasing of circumferential wave number. Fig. 4 shows the analysis of frequencies with ratio of height to radius ratios with two boundary conditions.

The results reveal a substantial increase in frequency predicted by the stress strain gradient theory underscoring the significant role of these effects in shaping the dynamic behavior of cylindrical shells. The frequency gap is very small between the curves of clamped-clamped and clamped-free frequencies.

CONCLUSION

In present work, cylindrical shaped shell has been investigated for frequency vibrations. The strain shell theory is used for the governing equations of the shell. The shell frequency vibrations have been achieved for different parameters. Results are acquired for different end point conditions. The frequencies decrease on increasing the L/R. For circumferential wave number, the frequencies increase. The frequency vibrations shell has been increased considerably with growing h/R ratios. Also, these have been increased for the number of axial waves. Moreover, this work has a wide range of applications in many fields such as in material science and it might be helpful in future investigation into different composite systems under various physical conditions

Declaration of Conflicting Interests

The author(s) declared no potential conflicts of interest with respect to the research, authorship, and/or publication of this article.

REFERENCES

Abazari, A. M., Safavi, S. M., Rezazadeh, G., and Villanueva. L. G. (2015, "Modelling the size effects on the mechanical properties of micro/nano structures", *Sensors*, 15(11),28543-28562. https://doi.org/10.3390/s151128543

Ahmadi, I. (2022), "Free vibration of multiple-nanobeam system with nonlocal Timoshenko beam theory for various boundary conditions", *Engineering Analysis with Boundary Elements*, 143, 719-739. https://doi.org/10.1016/j.enganabound.2022.07.011

Chung, H., Turula, P. Mulcahy, T. M., and Jendrzejczyk, J. A. (1981), "Analysis of cylindrical shell vibrating in a cylindrical fluid region", *Nuclear Engineering and Design*, 63(1), 109–1012. https://doi.org/10.1016/0029-5493(81)90020-0.

Dastjerdi, S. and M. Jabbarzadeh. (2017), "Non-linear bending analysis of multi-layer orthotropic annular/circular graphene sheets embedded in elastic matrix in thermal environment based on non-local elasticity theory", *Applied Mathematical Modelling*, 41, 83-101. https://doi.org/10.1016/j.apm.2016.08.022

Di Taranto, R. A. and Lessen, M. (1964), "Coriolis acceleration effect on the vibration of rotating thin-walled circular cylinder", Trans. ASME, *Journal of Applied Mechanics*, 31, 700 – 701. DOI: 10.1115/1.3629733

Ergin, A., and Temarel, P. (2002), "Free vibration of a partially liquid-filled and submerged, horizontal cylindrical shell", *Journal of Sound and vibration*, 254(5), 951-965. https://doi.org/10.1006/jsvi.2001.4139

Farahani, H. and F. Barati. 2015, "Vibration of sumberged functionally graded cylindrical shell based on first order shear deformation theory using wave propagation method" *Struct. Eng. Mech*. 53, 575-587.

Fleck, N., Muller, G., Ashby, M. F., and Hutchinson, J. W. (1994), "Strain gradient plasticity: theory and experiment", *Acta Metallurgica et materialia*, 42(2), 475-487. https://doi.org/10.1016/j.ijsolstr.2005.05.026

Gao, Y., and An, L. (2010), "A nonlocal elastic anisotropic shell model for microtubule buckling behaviors in cytoplasm" *Physica E: Low-Dimensional Systems and Nanostructures*, 42(9), 2406-2415.

Ghavanloo, E., H. Rafii-Tabar and S. A.Fazelzadeh. (2019), "New insights on nonlocal spherical shell model and its application to free vibration of spherical fullerene molecules", *International Journal of Mechanical Sciences*, 161, 105046. https://doi.org/10.1016/j.ijmecsci.2019.105046

Golpayegani, I.F. and E. Ghorbani. (2016), "Free vibration analysis of FGM cylindrical shells under non-uniform internal pressure*", J. Mater. Environ. Sci.* 7:981-992.

Hussain, M. and Selmi, A. (2020). "Analytical vibration of FG cylindrical shell with ring support based on various configurations." *Advances in concrete construction*, 9, 557-568.

Kaufmann, W., J. Mata-Falcón, M. Weber, T. Galkovski, T. Duc Thong and J. Kabelac, (2020), *Compatible stress field design of structural concrete*. ETH Zurich. 1601336954

Lam, D. C., Yang, F., Chong, A., Wang, J., and Tong, P. (2003), "Experiments and theory in strain gradient elasticity", *Journal of the Mechanics and Physics of Solids*, 51(8), 1477-1508. https://doi.org/10.1177/1081286508097638

Lam, K.Y., Loy, C.T., (!995), "Effects of boundary conditions on frequencies of a multi-layered cylindrical shell", J. SoundVib. 188, 363–384. https://doi.org/10.1006/jsvi.1995.0599

Li, H. and Lam, K. Y. (1998), "Frequency characteristics of a thin rotating cylindrical shell using the generalized differential quadrature method", *International Journal of Mechanical Science*, 40(5), 443-459. https://doi.org/10.1016/S0020-7403(97)00057-X

Loy, C. T., and Lam, K. Y. (1997), "Vibration of cylindrical shells with ring support" *International Journal of Mechanical Sciences*, 39, 455-471. https://doi.org/10.1016/S0020-7403(96)00035-5

Loy, C. T., Lam, K. Y., and Reddy, J. N. (1999), "Vibration of functionally graded cylindrical shells", *International Journal of Mechanical Sciences*, 41, 309-324. https://doi.org/10.1016/S0020-7403(98)00054-X

Malekzadeh, P., and Heydarpour, Y. (2012), "Free vibration analysis of rotating functionally graded cylindrical shells in thermal environment*", Composite Structures*, 94(9), 2971-2981. https://doi.org/10.1016/j.compstruct.2012.04.011

Najafizadeh, M. M. and Isvandzibaei, M. R. (2007), "Vibration of (FGM) cylindrical shells based on higher order shear deformation plate theory with ring support", *Acta Mechanica* 191, 75–91. http/10.1007/s00707-006-0438-0

Natsuki, T. and J. Natsuki. (2023), "Constitutive Modeling of Mechanical Behaviors of Carbon-Based CNTs and GSs, and Their Sensing Applications as Nanomechanical Resonators: A Review", *Nanomaterials*, 13(12), 1834. 2079-4991/13/12/1834

Penzes, R L. E. and Kraus H. (1972), "Free vibrations of pre-stresses cylindrical shells having arbitrary homogeneous boundary conditions",*AIAA Journal*, 10, 1309. https://doi.org/10.2514/3.6605

Rahmani, O., S. Norouzi, H. Golmohammadi and S. Hosseini. 2017, "Dynamic response of a double, single-walled carbon nanotube under a moving nanoparticle based on modified nonlocal elasticity theory considering surface effects", *Mechanics of Advanced Materials and Structures*, 24(15), 1274-1291. doi.org/10.1080/15376494.2016.1227504

Selmi, A. (2020), "Dynamic behavior of axially functionally graded simply supported beams", *Smart Structures and Systems*, 25, 669-678.

Şimşek, M. (2011), "Nonlocal effects in the forced vibration of an elastically connected double-carbon nanotube system under a moving nanoparticle", *Computational Materials Science*, 50(7), 2112-2123. 10.1007/s12206-012-0338-2

Sivadas, K. R. and Ganesan, N. (1964), "Effect of rotation on vibrations of moderately thin cylindrical shell", Journal of Vibration and Acoustics, 116 (1):198 – 202 (. DOI: 10.1115/1.2930412

Wang S. S. and Chen, Y. (1974), "Effects of rotation on vibrations of circular cylindrical shells", *Journal of the Acoustical Society of America*, 55, 1340 – 1342. https://doi.org/10.1121/1.1914708

Xiang, Y., Ma. Y.F., Kitipornchai. S., Lau. C.W.H. (2002), "Exact solutions for vibration of cylindrical shells with intermediate ring supports", International Journal of Mechanical Sciences, 44(9),1907-1924.

Xuebin, L. (2008), "Study on free vibration analysis of circular cylindrical shells using wave propagation", *J. Sound Vib*. 311, 667-682.

Yang, Y., and C. W. Lim. (2011), "A new nonlocal cylindrical shell model for axisymmetric wave propagation in carbon nanotubes", *Advanced Science Letters*, 4(1), 121-131. https://doi.org/10.1166/asl.2011.1177

Appendix-I

$$A_1 = (1-\mu_d^2\Theta^2\ ) \quad , \quad A_2 = (1-\mu_s^2\Theta^2\ )$$

$$a_1 = \frac{RhE_x}{1-\Upsilon_{\xi x}\Upsilon_{x\xi}},$$

$$a_2 = \frac{hE_x\Upsilon_{\xi x}}{1-\Upsilon_{\xi x}\Upsilon_{x\xi}}$$

$$a_3 = \frac{hG_{x\xi}}{R}, a_4 = hG_{x\xi}$$

$$b_1 = c_6 = \frac{hE_\xi}{1-\Upsilon_{\xi x}\Upsilon_{x\xi}}$$

$$b_2 = c_7 = \frac{hE_\xi}{R\left(1-\Upsilon_{\xi x}\Upsilon_{x\xi}\right)}$$

$$b_{3=}Ra_3$$

$$b_4 = \ \mathrm{R}a_4,\ c_1 = \ \left(\frac{Rh_o^3\,E_x}{12(1-\Upsilon_{\xi x}\Upsilon_{x\xi}}\right)$$

$$c_2 = \left(\frac{h_o^3\,E_x\Upsilon_{\xi x}}{12R(1-\Upsilon_{\xi x}\Upsilon_{x\xi}}\right)$$

$$c_3 = \left(\frac{h_o^3\,E_\xi\Upsilon_{x\xi}}{12R(1-\Upsilon_{\xi x}\Upsilon_{x\xi}}\right)$$

$$c_4 = \left(\frac{h_o^3\,E_\xi}{12R^3(1-\Upsilon_{\xi x}\Upsilon_{x\xi}}\right), c_5 = \frac{h_o^3 G_{x\xi}}{3R}$$

ISBN: 978-625-93265-1-1